POLITECNICO DI TORINO

Master degree
in Nanotechnologies for ICTs

Master Degree Thesis

Fabrication and characterization of 2D and 3D perpendicular nanomagnetic devices with CoFeB/MgO ultrathin films

Supervisors
prof. Marco Vacca
prof. Mariagrazia Graziano

Candidate
Diego Favaro

Academic Year 2020-2021

Summary

According to the International Technology Roadmap of Semiconductors (ITRS), the complementary metal-oxide semiconductor (CMOS) technology era is reaching its technological and economical limits. Several new approaches and technologies are investigated by industry and academia with the aim to replace the CMOS technology or to implement hybrid integrated circuits (ICs). Among these, perpendicular Nanomagnetic Logic (pNML) seems to be very promising. This technology can combine memory and logic computing capability in the same device, giving the possibility to overcome the von Neumann bottleneck. pNLM exploits nanomagnets able to store digital binary information (1 and 0) encoded in their bistable perpendicular magnetization state (up/down), and to directly modify these magnetic states by magnetic field interaction between neighboring magnets.
This work investigates the principles of pNML and proves the reliability of this technology, focusing on a new magnetic material stack, Ta/CoFeB/MgO/Ta ultra-thin film. This new stack should be more suitable than the previously investigated films, such as Co/Pt, Co/Ni, or Fe/Pt, for lower power and higher frequency logic operations. After the fabrication and characterization of the Ta/CoFeB/MgO/Ta magnetic structures, Focused Ion Beam (FIB) irradiation is performed to tune their magnetic properties, allowing to establish the correct coupling between the magnets and create working logic gates as inverters and majority voters. Design optimization is supported by micromagnetic simulations. Moreover, this thesis demonstrates the possibility to perform logic operations exploiting not only 2D architectures but also more complex and more performing 3D structures.

Acknowledgements

I would like to thank my professors from the Polytechnic of Turin, M. Vacca and M. Graziano, for the opportunity to join this exciting project.
This thesis is the result of an experimental research in the Nanomagnetic Device Group, Chair of Nano and Quantum Sensors, at the Technical University of Munich, with the support of the Central Electronics and Information Technology Laboratory - $ZEIT^{lab}$.
I would like to thank Prof.Dr.Ing M. Becherer for the great hospitality and for his involvement and guidance during the work.
I would like to say many thanks to my tutors in Italy, F. Riente e L. Gnoli, to my tutors in Germany, S. Mendisch and V. Ahrens, and to all the members of the $ZEIT^{lab}$ group (in a particular way, to A. Kwiatkowski and M. Küffner) .

Contents

List of Tables 6

List of Figures 7

1 Introduction 13

1.1 Beyond CMOS technology . . . 13

1.2 NML: Nanomagnetic Logic . . . 15

2 Principles of pNML 17

2.1 Micromagnetism . . . 17

2.2 Fundamentals of pNML . . . 24

3 New generation of pNLM device: CoFeB/MgO thin film 31

3.1 CoFeB/MgO interface . . . 31

3.2 Sample fabrication . . . 32

4 Engineered domain nucleation 37

4.1 Structures patterning . . . 39

4.2 Areal irradiation study . . . 40

4.2.1 Methodology . . . 41

4.2.2 Results . . . 42

4.3 ANC study . . . 44

4.3.1 Micromagnetic simulations . . . 44

4.3.2 Experimental results . . . 50

5 2D Logic device 53

6 3D Logic device 61
6.1 Sample fabrication and structures patterning 63
6.2 Irradiation study 69
6.3 The single input gate 73
6.4 The double input gate 77

7 Conclusion 85

Appendices 87

A Experimental set-up 89
A.1 Magneto-optical microscopy 89
A.1.1 Laser-scanning MOKE 89
A.1.2 Wide-field MOKE 90
A.2 Focused ion beam 90

B Fabrication process parameters 93
B.1 2D logic device 93
B.2 3D Logic device: 95

List of Tables

3.1 *Sputtering parameters* 33
4.1 *Magnetic parameters implemented in the simulations* 45
5.1 *Coupling field results* 59
6.1 *Coupling field results (sample A4)* 76
6.2 *Coupling field results* 82

List of Figures

1.1 *Magnetization vector directions: comparison between iNML and pNML (image taken from [19]).* . . . 16

2.1 *Domain wall classification* . . . 21

2.2 *Vector description of the LLG equation (image taken from [5]).* . . . 24

2.3 *pNML: output magnet switching process (image taken from [3]).* . . . 25

2.4 *DW velocity versus the applied magnetic field in magnetic multilayer with PMA. The dashed line represents the DW velocity in an ideal ferromagnet (image taken from [14])* . . . 26

2.5 *Artificial pinning sites.* . . . 27

3.1 *Laser MOKE image: as deposited state. The image on the left represents the output signal of the MOKE and the magnetic field measured by the sensor over the time. On the left instead, the hysteresis.* . . . 33

3.2 After annealing: a) Hysteresis measured by the LMOKE b) Magnetic domains imaged by the WMOKE (50x objective). . . . 35

4.1 *a) CAD model of a box containing the test structures to pattern for the irradiation study b) WMOKE image of the patterned test wires (50x objective).* . . . 39

4.2 *Ga^+ dose dependent evolution of the saturation magnetization M_s and coercivity H_c (image taken from [11]).* . . . 40

4.3 *Sketch of the train of pulses implemented for the switching field measurement by WMOKE.* . . . 41

4.4 *Areal irradiation results: switching field comparison before (red curve) and after background irradiation (blue curve). Each point of the plots is referred to a wire belonging to a certain box illuminated with the corresponding dose (five boxes, five different ions doses).* . . . 42

4.5 *Areal irradiation results: switching field difference (after irradiation - before irradiation). The red-dashed line is a reference to highlight the zero value.* 42
4.6 *Simulated structures: a) squared ANC (50 nm side) in the center, b) squared ANC (50 nm side) at the border, c) circular ANC (56.4 nm diameter) at the border. The wire is 400 nm long, has width of 80 nm and is thick 1 nm.* 45
4.7 *Hysteresis comparison of a wire with the ANC placed at the border (blue curve) and at the center (red curve). Structures represented in fig.4.6* (a) and (b) 46
4.8 *Hysteresis in case of squared and circular ANC placed at the border. The simulated structures are shown in fig.4.6 (b) and (c).* 47
4.9 *Magnetization dynamics of the simulated disk: evolution of m_z over time under different field angles with respect the out-of-plane direction.* 48
4.10 *Simulated switching dynamics, $\theta = 10\,°$. Sequence of images which show how the switching process of the magnet evolves over time.* . . . 49
4.11 *Switching dynamics, $\theta = 70°$.* Sequence of images which show how the switching process evolves over time. 49
4.12 *CAD model for the ANC irradiation* 50
4.13 *ANC study results: switching field comparison before (red curve) and after irradiation (blue curve). The irradiation consists in the global areal irradiation (fixed at $2.25 \cdot 10^{13} \frac{ions}{cm^2}$) plus the local irradiation for the ANC creation. The values on the x-axis are referred to the cumulative ions dose in the ANC region.* 51
4.14 *ANC study results: switching field difference (after irradiation - before irradiation). The red dashed curve is a reference which represents the zero value.* 51
5.1 *Micromagnetic simulation of an inverter in the case in which the inversion is supported (upper row) and prevented (bottom row). The magnetic parameters of the structure are listed in table4.1. The input has a fork-like structure to surround the ANC and maximize the efficiency of the coupling. The dimensions are 0.7 µm x 1 µm, the gap is 100 nm as the width of the output and the ANC is a square of 50 nm side placed in contact with the left border of the output. In this simulation, temperature and grains are taken into account.* 54

5.2 *CAD model for the inverters FIB lithography process: a) Complete FIB lithography mask, b) Zoom of an inverter showing the common size in μm. The structure on the left is the input, the one on the right the output. The input has a length of 700 nm and a width of 1 μm, while the total length of the output is 1.8 μm and the width of the narrower region is 100 nm.* 56
5.3 *a) WMOKE (50x objective) image of a FIB lithography patterned box containing 30 inverters, b) AFM image of an inverter with nominal gap of 100 nm (real gap $\sim$ 150 nm)* 56
5.4 *Working inverters results: switching field behaviour of input (blue curve) and output (red curve) before and after the irradiation steps* 57
5.5 *Coupling measurement train of pulses set up* 58
5.6 *Coupling measurement result for the twelve working inverters. In blue the measured switching field of the output in the supported configuration, while in red, the result in the prevented configuration* . . 59
6.1 *Simulated structures: the simulated structures are wires of 400 nm length, width of 80 nm and a thickness of 1 nm. The grid dimension is 256 x 256 x 1 and the size of a single cell is 2.5 nm x 2.5 nm x 1 nm.* 62
6.2 *Coupling field comparison: The curves represent the stray field distribution in the output. The stray field generated by the inputs in the 3D layout (red curve) and 2D layout (blue curve) is plotted along the x-direction (width of the output) at the cross section (y=constant) corresponding to the middle of the output.* 62
6.3 *Sketch of the sputtered double layer sample.* 63
6.4 *Sketch of the patterned 20 μm x 20 μm squares after the photolithography and the Ar^+ etching process.* 64
6.5 *Sketch of the final patterned structures after the FIB lithography and the Ar^+ etching process. From the left to the right: the single input layer structure, used as test structure for the irradiation study, the single island structure and the double island structure.* 65
6.6 *Gap between the two top island imaged by AFM (square A12)* . . . 66
6.7 *AFM analysis of the gap (square A12). The result shows a measured gap of 152 nm (the nominal distance was 150 nm).* 66

6.8 *Hysteresis of a single layer structure (square D17). The image on the left represents the output signal of the MOKE and the magnetic field measured by the sensor over the time. On the left instead, the resulting hysteresis.* . . . 67

6.9 *Hysteresis on top of the single island (square C17). The image on the left represents the output signal of the MOKE and the magnetic field measured by the sensor over the time. On the left instead, the resulting hysteresis.* . . . 68

6.10 *Areal irradiation results: switching field comparison and difference before and after the areal irradiation step, for different ions doses. This irradiation analysis is performed on the single layers structures.* 69

6.11 *Areal irradiation results: switching field comparison and difference before and after the areal irradiation step, for a selected ion dose* ($t_{dwell} = 1.5\mu s$) . . . 70

6.12 *Comparison between two single layer squares with an overlapped mask for FIB areal irradiation of 19 μm x 19 μm (on the left) and one of 10 μm x 10 μm (on the right).* . . . 71

6.13 *ANC creation results: switching field comparison and difference before and after the ANC creation, for different ions doses. The structures under test are the twenty magnets (J00-J19) already irradiated with an areal irradiation of* $1.5\mu s$ *(fig.6.11)* . . . 72

6.14 *Top view image of the single input device imaged by WMOKE microscope. The yellow arrow indicates where the ANC should be placed.* 73

6.15 *Hysteresis measurement of the bottom layer (sample A4) by Laser MOKE. The image on the left represents the output signal of the MOKE and the magnetic field measured by the sensor over the time. On the left instead, the resulting hysteresis.* . . . 74

6.16 *Laser MOKE output 50 cycles hysteresis results for both input logic configurations (sample A4). The blue histograms represent the count of the switching events, while the red line is referred to the mean values of the switching field distribution (indicated as coercivity and defined as* H_c^+ *and* H_c^- *in table 6.1).* . . . 75

6.17 *Top view image of two double input devices (called A12 and A13) imaged by WMOKE microscope.* . . . 77

6.18 *Hysteresis loop measure of the output by Laser-MOKE (sample A12). The image on the left represents the output signal of the MOKE and the magnetic field measured by the sensor over the time. On the left instead, the resulting hysteresis.* 79
6.19 *Hysteresis loop measure of the two inputs by Laser-MOKE (sample A12). The image on the left represents the output signal of the MOKE and the magnetic field measured by the sensor over the time. On the left instead, the resulting hysteresis.* 79
6.20 *WMOKE images of the sample A12 (the left one) in different logic configurations.* 80
6.21 *Hysteresis loops analysis: case 0,1. The blue histograms represent the count of the switching events over the 50 hysteresis measurements, while the red line is referred to the mean values of the switching field distribution.* 80
6.22 *Hysteresis loops analysis: case 1,0. The blue histograms represent the count of the switching events over the 50 hysteresis measurements, while the red line is referred to the mean values of the switching field distribution.* 81
6.23 *Hysteresis loops analysis: case 0,0. The blue histograms represent the count of the switching events over the 50 hysteresis measurements, while the red line is referred to the mean values of the switching field distribution.* 81
6.24 *Hysteresis loops analysis: case 1,1. The blue histograms represent the count of the switching events over the 50 hysteresis measurements, while the red line is referred to the mean values of the switching field distribution.* 82
A.1 *Schematic diagram of FIB column architecture (image taken from "Micrion 9000/9100/9.5 00 Focused Ion Beam Systems Operation Manual")* 92

1 Introduction

In the last 50 years, the evolution of CMOS and ICs technology was ruled by the Moore's law, which states that the number of integrated components on integrated circuits doubles every two years. This trend is based on the scaling of the dimensions of the single transistor. The main results were an exponential decrease in term of cost and an exponential increase in term of performances. This direction allowed to move from the 10 μm node in 1971 to the most recent 5 nm node, but due to unavoidable physical limits, it can not be maintained continuously. To reduce the size is leading to many device fabrication problems, in term of power dissipation, reliability, temperature and manufacturing costs. New different approaches, called "*More than Moore*" and "*Beyond CMOS*", have started to be investigated with particular efforts in the recent years.

1.1 Beyond CMOS technology

The International Technology Roadmap Of Semiconductor defines the beyond CMOS technology as a class of logic and information processing devices with the aim to extend and partially substitute the CMOS technology. To be reliable replacements, these devices have to fulfill different requirements in term of scalability, delay and power dissipation. Moreover, they should operate at room temperature, have low fabrication variability and be compatible with CMOS architecture and processes. But the most important prerequisite concerns the logic. In particular, these devices must provides concatenation, feedback prevention and the complete set of Boolean logic operators (NOT, AND, OR). The new devices belonging to the beyond CMOS technology are classified in three categories:

- Extended field effect transistor (FETs): they exploit the well known MOSFET technology trying to improve its functionality with novel channel materials, like graphene, carbon nanotubes or semiconducting nanowires.

- Non conventional FETs and other charge based devices: The input signal is still a current or a voltage, but novel materials are implemented. An example are the Spin-FET, in which drain and source are made by ferromagnetic materials.

- Non conventional FETs and non charge based devices: they are made by novel material and use unconventional way to implement the logic state and bias signals. Examples are spin wave devices and NML.

These devices should be able not only to provides the possibility of scaling and miniaturization, but also a new computational architecture that can combine in a single device memory and logic operations. This last feature would be an important improvement with respect the CMOS technology, allowing to overcome the von Neumann bottleneck. Magnetic devices can offer the feasibility to fulfill both the characteristics:

- A bistable remanent magnetization state which can be used to encode and store binary information (1 and 0).

- The generation of a stray field which couples the magnetic units and allow to perform logic operation.

This work is focused on the last of the previously mentioned classes and in particular on the Nanomagnetic Logic.

1.2 NML: Nanomagnetic Logic

The origin of the NML can be attributed to the exploration of the Quantum Cellular Automata (QCA). This technology exploited the Coulomb interaction between electrons belonging to different quantum cells to perform logic operations. The fundamental step towards the NML was done in the year 2000, when Cowburn and Welland [4] implemented QCA with magnets (MQCA). Small magnetic dots made of Permalloy were used as quantum cells and their stray field exploited for the interaction and modification of the logic state encoded in their magnetization. NML exploits magnets in which is possible to store binary information and which are able to interact between each other thanks to dipole magnetic field generated by them self. This coupling field influences the neighboring magnets, supporting or preventing their magnetization switch, giving the basis to perform logic operations. The most important features of NML that make it a good candidate for beyond CMOS applications are:

- Non-volatility of the stored data
- Possibility of integration with standard CMOS technology
- Absence of interconnections

NML technology has two possible implementations depending on the orientation of the magnetization with respect to the surface of the magnet: in-plane NML (iNML) and perpendicular NML (pNML). In iNML the magnetization is parallel to the magnetic surface, while in pNML it is perpendicular to it (out of plane magnetization). In contrast with iNML which use Permalloy with dominant shape anisotropy, the magnetic behaviour of perpendicular nanomagnets made of Co/Pt, Co/Ni and the most recent CoFeB, is ruled by crystalline and interface anisotropy. Another important difference between the two implementations is the role of the clocking field. In iNML the clock field induced a reset state in the magnetization (high energy state) and after the release of the bias, the magnetization turns following the lower energy states depending on the magnetic environment defined by the neighboring magnets. In pNML instead, there is not a reset state. The external field is used to nucleate a new domain in the output and to propagate it through the domain wall motion along the whole magnet, switching its magnetization state. This study is focused on pNML. It provides few advantages with respect to the in-plane implementation [25]. The limit of iNML is that, after few nanomagnets, the encoded information becomes unstable due to physical non-idealities (as thermal noise). For this reason, is required to divide the logic circuit into clock zone in which the maximum number of magnetic unit is limited and in this way, the signal propagates through a multi-phase clocking system. pNML overcomes this limit thanks to its intrinsic physical properties and only one clock signal is applied to the whole circuit, introducing the advantages of a more compact system and a simpler design.

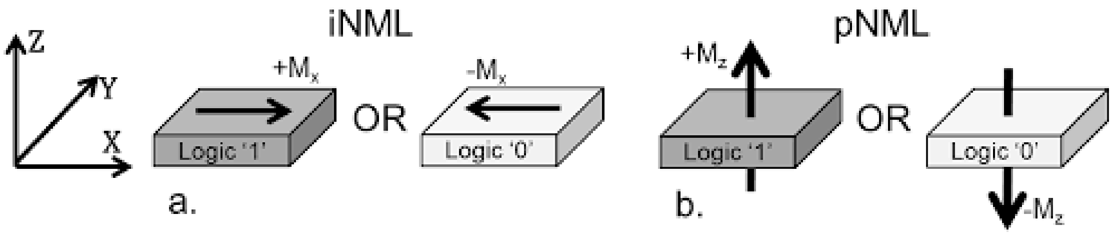

Figure 1.1: *Magnetization vector directions: comparison between iNML and pNML (image taken from [19]).*

2 Principles of pNML

The goal of this thesis is to demonstrate the possibility to build reliable logic device made by nanomagnets with perpendicular magnetic anisotropy (PMA). In this chapter, the fundamentals of pNML and the main physical effects and equations behind the magnetic properties engineered to perform logic operations are briefly discussed (for more detailed information about the theory, the reader is referred to these references: [1], [2]).

2.1 Micromagnetism

The micromagnetic theory is a bridge between the macroscopic Maxwell's theory and the quantum theory. Micromagnetism is based on the minimization of the energy related to the magnetization vector. This minimum is reached through the generation of a torque on the magnetization vector, which turns its spatial orientation [1]. The total energy of a magnet has different contributions coming from different interactions:

$$E_{tot} = E_{exch} + E_{ani} + E_{Zeeman} + E_{demag} + E_{th} + E_{ms} + E_{me} \tag{2.1}$$

Exchange energy

Exchange interactions are the responsible of long range order in the material. They are electrostatic interactions between two neighboring spins, called $\mathbf{S}_i$ and $\mathbf{S}_j$, which tend to align them self into a parallel magnetization direction [9]. The exchange energy is described by the formula:

$$E_{exch} = -2J_0\mathbf{S}_i \cdot \mathbf{S}_j = -2J_0 S_i S_j \cos\phi \tag{2.2}$$

Where J_0 is the exchange constant, $\mathbf{S}_{i,j}$ are the spin vectors and ϕ is the angle between them. Due to the presence of the minus sign, this energy contribution is minimized when the spins are parallels ($\phi = 0$ and $\cos\phi = 1$). For a bulk material, the exchange energy of a pair of spin is integrated over the bulk volume V, and eq. 2.2 becomes:

$$E_{exch} = A \int_V (\nabla \mathbf{M}(\mathbf{r}))^2 dV \tag{2.3}$$

$\mathbf{M}$ is the magnetization vector, which depends on the position $\mathbf{r}$ and A is the exchange stiffness, a material constant which describes how strongly two neighboring spins tend to stay parallel aligned.

Anisotropy energy

In the absence of an external magnetic field, the magnetization vector tends to align along an energetic favourable direction called *easy axis* (*hard axis* instead is the most energetic one). The electrons orbitals are linked to the magnet crystallographic structure and their interaction with the spins makes the last to prefer to align along a certain crystallographic direction. The fact that the magnetization lies on a specific direction with respect to the crystallographic structure is called *magnetic anisotropy*. The energy related to this magnetic property has different contributions:

- **Magnetocrystalline anisotropy**
  The magnetocrystalline anisotropy, called also uniaxial anisotropy, derives from spin-orbit interactions and the energy related depends on the angle θ between the magnetization vector and the easy axis [2]:

$$E_{ani,u} = \int (K_{u1} \sin^2\theta + K_{u2} \sin^4\theta) dV \tag{2.4}$$

  With K_{u1} and K_{u2} defined as uniaxial anisotropy constant, while V is the volume of the magnetic material. Here, the energy minimum is reached when the magnetization vector is parallel or a antiparallel with respect to the easy axis ($\theta = 0$ or $\theta = \pi$).

- **Shape anisotropy**
  The origin of the shape anisotropy lies in the long-range dipole-dipole interaction. This interaction generates a magnetic field, called *stray field*, which counteracts the magnetization [6]. The corresponding energy is:

$$E_{ani,s} = \frac{\mu_0}{2} V \mathbf{MNM} \tag{2.5}$$

Where V is the volume, **M** is the magnetization vector and **N** is the demagnetizing tensor, which contains the dependency on the geometrical shape. Magnetic thin film can be approximated as a spheroid due to the higher lateral extension with respect to the thickness, and the previous formula can be rewritten as:

$$E_{ani,s} = \frac{\mu_0}{2} V M^2 \cos^2\theta \tag{2.6}$$

θ is the angle between **M** and the vector normal to the surface. This means that this contribution tends to orient the magnetization vector parallel to the surface plane (energy minimized for $\theta = \pm\frac{\pi}{2}$).

- **Interface anisotropy**
  This contribution arises in multi-layer structures, when the symmetry of the crystallographic structure is broken at the interface between ferromagnetic and non-magnetic materials. The related energy contribution is defined as:

  $$E_{ani,i} = \int K_i[1 - (\mathbf{M} \cdot \mathbf{n})^2] dA \tag{2.7}$$

  This energy is minimized when the magnetization is parallel to the surface normal, i.e perpendicular magnetization.

Demagnetization energy

The demagnetization energy contribution is related to the intensity of the stray field:

$$E_{demag} = \frac{\mu_0}{2} \int_{space} H^2_{demag} dV = -\frac{1}{2} \int_{magnet} \mathbf{M} \cdot \mathbf{H}_{demag} dV \tag{2.8}$$

The origin of the stray field can be tracked in the divergence of the magnetization [9]. When the magnetization vector meets a surface, it is suddenly stopped and the magnetic monopoles left on the surface generates an opposite field $\mathbf{H}_d$. If one consider a magnet with an infinite lateral extension, this energy contribution will tend to orient the magnetization vector in-plane. In this configuration, the magnetization divergence is only at the ends of the magnet, supposed to be at infinite distance, and the demagnetizing field will be equal to zero. If instead the magnetization is perpendicular to the surface, a lot of magnetic monopoles will be generated on the upper and bottom surface of the magnet, giving rise to a strong stray field. This energy contribution is directly linked with the shape anisotropy. Depending on the shape of the structure, the magnetization vector will lie along the direction which minimized the most the charge density on the surface [2].

Zeeman energy

The Zeeman energy originates from the interaction of the magnetization vector and an applied external field.

$$E_{Zeeman} = -M_s \int \mathbf{H}_{ext} \cdot \mathbf{M} dV \tag{2.9}$$

To minimize this contribution, the magnetization vector tends to align along the field direction. There are other energy contributions as the thermal energy E_{th}, the magnetoelastic E_{me} and the magnetostrictive energy E_{ms}.
The magnetic texture of a magnet is the result of the competition of all these energy contributions [2]. The reason of the presence of *magnetic domains* (regions with parallel magnetization) in ferromagnetic materials derives from the minimization of the demagnetization energy [2]. More the magnetic structure is divided into domains of opposite magnetization, less is the stray field and the energy related to it. But the number of domains is not infinite. The regions of transition between domains, called *domain walls*, are energetic regions in which the magnetization vector rotates from one direction to the opposite one. Rotating, at a certain point, it lies along the hard axis direction, which costs energy [2]. This energy cost per unit of area is defined as:

$$\sigma_{DW} = \frac{NKa}{2} \tag{2.10}$$

N is the number of site in which the spins rotate, a is the lattice constant and K the anisotropy constant. Smaller is the width of the domain wall (lower N), less magnetic moments will be aligned along directions different from the easy axis, reducing the anistropy energy contribution [2]. On the other hand, a small number of atoms in the domain wall means that the variation direction between two consecutive magnetic moment is high, leading to an increase in the exchange energy [2]. Hence, another energy term related to the exchange interaction must be added in the domain wall energy formula:

$$\sigma_{DW} = \frac{NKa}{2} + J_0 S^2 \frac{\pi^2}{Na^2} \tag{2.11}$$

Minimizing this energy, is possible to extrapolate the equation that describes the domain wall width:

$$\delta = \pi S \sqrt{\frac{2J}{Ka}} = \pi \sqrt{\frac{A}{K}} \tag{2.12}$$

This result tells that the exchange interactions favor a broad domain wall, while the anisotropy tends to shrink its size. Therefore, the width of a domain wall is defined by the balance between the exchange and anisotropy energies, while the formation of domains, by the balance between the demagnetizing energy and the energy cost to create a new domain wall [2]. The domain wall are classified according to the angle between the magnetization of two neighboring domains. A 180° wall separates two domains with opposite magnetization, a 90° wall, two domains with perpendicular magnetization (fig.2.1 (a)). Between the 180° wall, is possible to distinguish two types of domain wall depending on how the magnetization rotates. One possible configuration is the *Bloch wall*, in which the magnetization rotates in a plane parallel to the plane of the wall. The other is the *Nèel wall*, in wich the magnetization rotates in a plane perpendicular to the wall (fig.2.1(b)) [2].

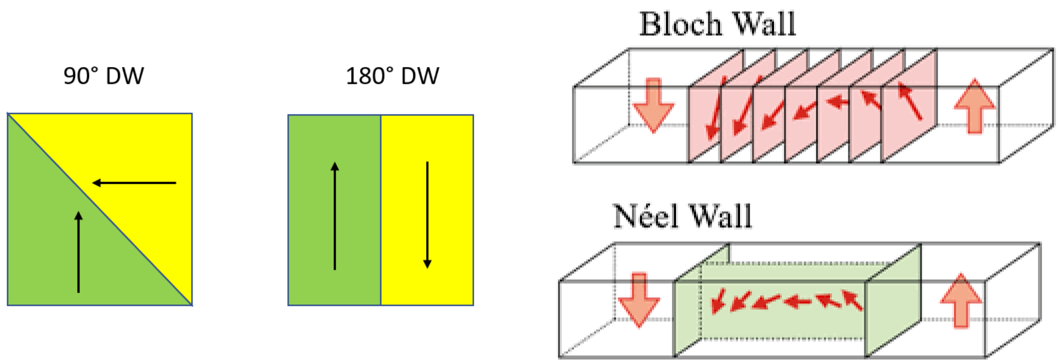

(a) *90° and 180° domain walls* (b) *180° walls: Bloch and Nèel wall (image taken from [16])*

Figure 2.1: *Domain wall classification*

This study deals with magnetic multi-layers samples. The thickness of this layers is nanometric, which means that the contribution of the interface anisotropy becomes important [10]. If its strength overcomes the shape anisotropy, the easy-axis rotates from in-plane to out-of plane, leading to the development of the *perpendicular magnetic anisotropy* (PMA). Usaully, all the anisotropy energy contributions are combined in a single term called *effective anisotropy energy* and its density is defined as [9]:

$$\epsilon_{ani} = K_{eff} \sin^2 \theta \tag{2.13}$$

K_{eff} is the effective anisotropy constant and θ is the angle between $\mathbf{M}$ and the surface normal. The effective anisotropy constant can be written considering all the previously mentioned anisotropy contributed as follow [12]:

$$K_{eff} = K_u - \frac{1}{2}\mu_0 M_s^2 + \frac{2K_i}{t_{layer}} \tag{2.14}$$

Where t_{layer} is the thickness of the ferromagnetic layer.
When $K_{eff} > 0$ the effective anisotropy energy is minimized for $\theta = 0$ or π, which means that the easy-axis turns out of plane and the material develops the PMA. When instead $K_{eff} < 0$, the easy-axis is in-plane being the energy minimized for $\theta = -\frac{\pi}{2}$ or $\frac{\pi}{2}$ [12]. Another important parameter that derives from the minimization of energy is the *critical domain diameter* D_{crit}:

$$D_{crit} = \frac{72\sqrt{AK_{eff}}}{\mu_0 M_s^2} \tag{2.15}$$

It defines the maximum possible feature size to have the single domain state, which is fundamental to store the information [2]. Above that, the multi-domain configuration is more energetic favourable.
In order to understand how the magnetization vector dynamics evolves in time to reduce the energy of the system, is important to briefly discuss the magnetic and mechanical properties of a moving electron [2]. Bohr defined the atomic magnetic moment from the current generated by an electron circulating around the nucleus of an atom:

$$m_d = IA = -\frac{e\omega_0}{2}r^2 \tag{2.16}$$

Where r is the orbit radius, ω_0 the circular frequency and e is the electron charge. The nucleus exerts a force on the electron, generating an angular momentum **L**:

$$L = \omega_0 m_e r^2 \tag{2.17}$$

with m_e the electron mass. The magnetic moment and the angular momentum are linked by a quantity called *gyromagnetic ratio*:

$$\mathbf{m}_d = \gamma L \tag{2.18}$$

Taking in consideration also the magnetic moment from the electron spin, the previous formula becomes:

$$\mathbf{m}_d = g\gamma L \tag{2.19}$$

Where g is the Lande gyromagnetic splitting factor. When an external field ($\mathbf{H}_{ext}$) is applied, a torque force **T** acts on the magnetic moment:

$$\mathbf{T} = \mu_0 \mathbf{m}_d \times \mathbf{H}_{ext} \tag{2.20}$$

This torque leads the magnetic moment to precess around the magnetic field direction. The torque can be also seen as the time derivative of the angular momentum, and eq. 2.18 can be rewritten as:

$$\mathbf{T} = \frac{dL}{dt} = \frac{1}{g\gamma}\frac{d\mathbf{m}_d}{dt} = \mu_0 \mathbf{m}_d \times \mathbf{H}_{ext} \tag{2.21}$$

From this formula, the basic equation of motion of the magnetization vector is derived:

$$\frac{d\mathbf{M}(\mathbf{r},t)}{dt} = -\gamma_{LLG}[\mathbf{M}(\mathbf{r},t) \times \mathbf{H}_{ext}(\mathbf{r},t)] \tag{2.22}$$

This equation describes the precession motion of $\mathbf{M}$ around $\mathbf{H}_{ext}$ without take into account the dissipation. Without dissipation, the magnetization precession would never stop. The Ohmic dissipation term that must be add to eq. 2.22 is:

$$\left(\frac{d\mathbf{M}(\mathbf{r},t)}{dt}\right)|_{diss} = \frac{\alpha}{M_s}[\mathbf{M}(\mathbf{r},t) \times \frac{d\mathbf{M}(\mathbf{r},t)}{dt}] \tag{2.23}$$

Where α is the damping constant and M_s the saturation magnetization. Summing all the contribution, the final equation becomes:

$$\frac{d\mathbf{M}(\mathbf{r},t)}{dt} = -\gamma_{LLG}[\mathbf{M}(\mathbf{r},t) \times \mathbf{H}_{eff}(\mathbf{r},t)] - \frac{\alpha\gamma_{LLG}}{M_s}[M(\mathbf{r},t) \times M(\mathbf{r},t) \times \mathbf{H}_{eff}(\mathbf{r},t)] \tag{2.24}$$

This equation is known as the *Landau-Lifshitz equation* (LLG) and describes the time variant magnetization dynamics under an effective field ($\mathbf{H}_{eff}$). The first term is referred to the precession motion, while the second to the damping. In the final eq. 2.24 the external field $\mathbf{H}_{ext}$ is replaced by the more general effective field, which takes into account different contributions, as the demagnetizing field, the field generated by the exchange interactions, the anisotropy field and the thermal field:

$$\mathbf{H}_{eff} = \mathbf{H}_{ext} + \mathbf{H}_{demag} + \mathbf{H}_{exch} + \mathbf{H}_{ani} + \mathbf{H}_{th} \tag{2.25}$$

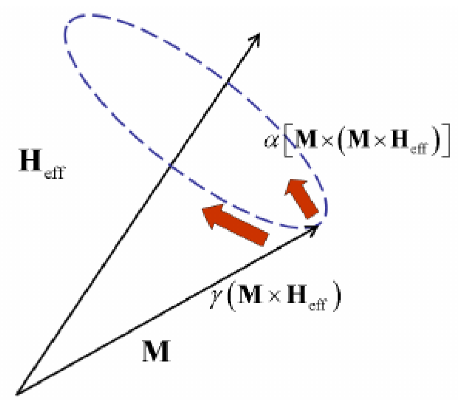

Figure 2.2: *Vector description of the LLG equation (image taken from [5]).*

2.2 Fundamentals of pNML

Perpendicular Nanomagnetic Logic exploits single domain nanomagnets with perpendicular magnetic anisotropy (PMA). They posses a bistable out of plane magnetization state which encodes the Boolean logic states 1 and 0. Neighboring magnets can interact by field coupling giving the possibility to realize Boolean logic functions. This technology provides a tunable switching mechanism, a controllable direction propagation of the signal and the feasibility to build 3D structure and architecture.

The physical phenomenon at the basis of the information retantion and transmission is the *switching process* of a nanomagnet. The switching process is characterized by the *nucleation* of a new domain and by the following propagation of its domain walls through the whole structure. Hence, in order to calculate the switching time of the magnet, both the nucleation time and the propagation time must be taken into account:

$$t_{switch} = t_{nuc} + t_{prop} \tag{2.26}$$

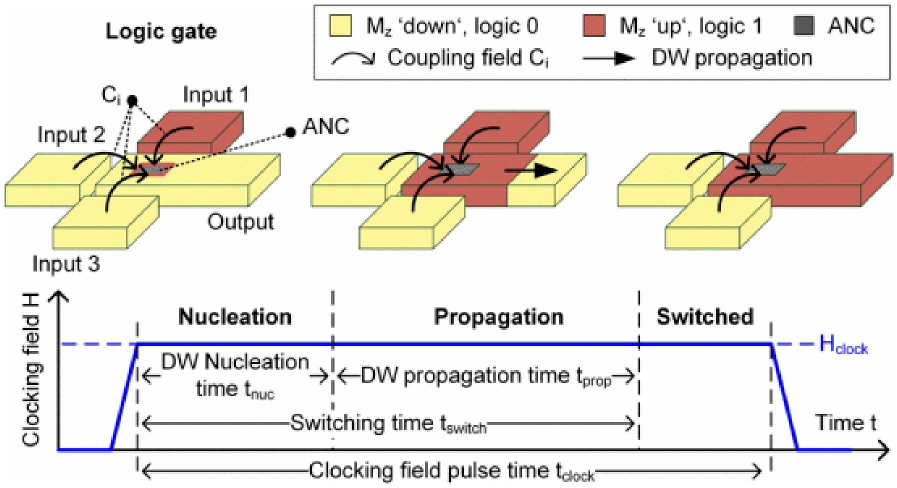

Figure 2.3: *pNML: output magnet switching process (image taken from [3]).*

Even if the complete magnetization reversal of a multi-layer structure is not coherent, it starts with the nucleation of a new domain in a small spot in the material. The domain nucleation is a coherent reversal process and it can be modeled by the Stoner-Wohlfarth model [23]. This model defines the field required to switch the magnetization of an area with effective anisotropy K_{eff}:

$$H_{ani} = \frac{2K_{eff}}{\mu_o M_s} \tag{2.27}$$

This field is called *anisotropy field*. Consequently, the magnetization reversal event generally occurs in the regions of lowest anisotropy, which are randomly distributed in the sample. To control the nucleation and the switching, Focused Ion beam irradiation (A) is widely used to create a local region of lowered anisotropy, called *artificial nucleation center* (e.g. [11] , [12]). The clock field required to nucleate the new domain in the ANC is the main parameter which affect the power consumption. The clocking frequency and so, the speed of the device, is instead mainly dependent on the propagation of the domain along the whole structure. The propagation of the new domain under an external field (usually lower then the one required for the nucleation) implies the motion of a domain wall. This motion is the direct consequence of the minimization of the Zeeman energy and it is characterized by a velocity, called domain wall velocity.

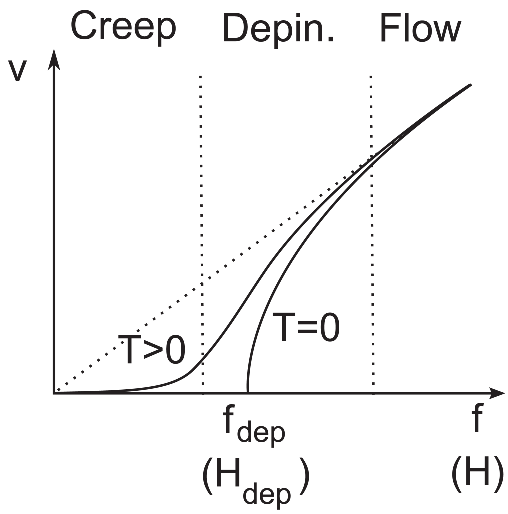

Figure 2.4: *DW velocity versus the applied magnetic field in magnetic multi-layer with PMA. The dashed line represents the DW velocity in an ideal ferromagnet (image taken from [14])*

Fig.2.4 shows the behaviour of the domain wall velocity with respect to the applied external magnetic field. The diagonal dashed line represents the velocity behaviour in case of an ideal ferromagnet. Without crystallographic defects and disorder, the relationship would be simply:

$$v_{DW} = \mu_w H \tag{2.28}$$

Whit μ_w the domain wall mobility. In the real case instead, the domain wall velocity has a non linear dependence on the external field, and depending on its value, different regimes of motion can be defined.

- **Creep regime:** This regime occurs for very small value of external field. The domain walls are pinned at the defects and the motion is random thermally activated. Anyway, the clock field are usually much larger then H_{dep} and this mechanism is irrelevant for pNML application.

- **Depinning regime:** For applied field higher then H_{dep} the velocity increases exponentially with the field. The motion is still thermally activated and the velocity strongly depends on the T.

- **Flow regime:** In the flow regime the field is much higher then H_{dep} and the crystallographic disorder and the temperature become irrelevant. The velocity has a linear relationship with the clock field:

$$v_{DW} = v_0 \mu_w (H - H_{dep}) \tag{2.29}$$

- **Saturation:** After a certain field, the so called Walker limit, the velocity saturates.

$$H_{Walker} = \frac{1}{2}\alpha M_s \tag{2.30}$$

  In particular, above this field value, the domain wall velocity may fluctuate or even oscillate. This behaviour is due to the coexistence of two senses of spin precession. When the effective field is high, the spin inside a Bloch wall start to rotate around the field direction, involving also the Nèel type wall. The harmony between the two types of wall generates oscillation in the wall velocity.

Important concepts for pNML operation are the *Pinning* and *Depinning* [21]. The pinning means the the domain wall is blocked by something and can not move. In other words, there is an energy barrier that opposes to the wall motion [21]. This energy barrier can be introduced by crystallographic defects and impurities, or by an anisotropy gradient [8]. To depin the domain wall, this energy barrier must be overcome, and it can be done trough the application of an external field (Zeeman energy), a current, or by the temperature (thermal energy). An engineered pinning and depinning of the domain propagation can allow to store information and synchronize information in complex pNML circuits. Artificial pinning sites can be introduced creating physical and geometrical deformation, called *notches* [21], or by anisotropy gradient generated by FIB irradiation, called *barriers* .

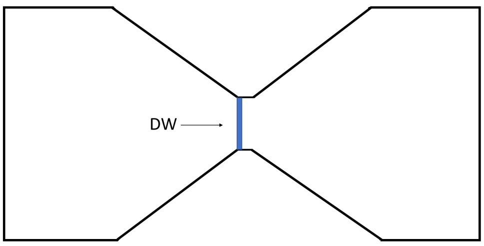

(a) *Notch*

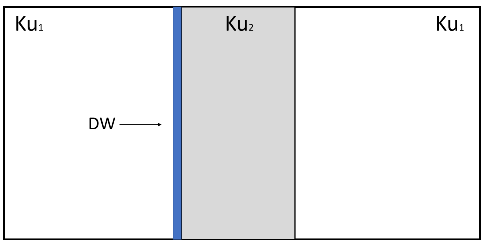

(b) *Barrier*

Figure 2.5: *Artificial pinning sites.*

In order to have an error free operation of a pNML circuit, the switching event of the magnet has to be completed during the clocking field pulses, bringing to the following constrain [3]:

$$t_{switch} = t_{nuc} + t_{prop} < t_{clock} \tag{2.31}$$

So, to calculate the switching time of a magnet and the relate clocking frequency, both the nucleation time and the propagation time must be taken into account. The domain nucleation at the ANC is influenced by the neighboring input magnets. The result is a superposition of coupling fields that must be added to the clock field, locally increasing or decreasing the effective field applied in the region of the ANC.

$$\mathbf{H}_{eff} = \mathbf{H}_{clock} - \sum M_i \mathbf{C}_i \tag{2.32}$$

Where $\mathbf{C}_i$ are the coupling fields and M_i the magnetization of the corresponding input (M $\in \{-1,1\}$). One of the most important parameter which describes the reliability of a pNML circuit is the *nucleation probability* P_{nuc}. It gives the probability to have a nucleation in the ANC with an effective field $\mathbf{H}_{eff}$ in an effective time t_{eff} and it is modeled by an Arrhenius switching model:

$$P_{nuc}(t_{eff}, H_{eff}) = 1 - \exp\left(\frac{-t_{eff}}{\tau(H_{eff})}\right) \tag{2.33}$$

With τ the inverse of the switching rate. The effect of the coupling fields is to increase or decrease dramatically this nucleation probability. If a magnet should not switch during a computation, the coupling fields have to prevent the domain nucleation during the clocking time, delaying the nucleation time (t_{nuc}) above t_{clock}. If instead the switch is required, they should support the clocking field, reducing the nucleation time . The conditions for a reliable logic operation are:

$$P_{supported} = P_{nuc}(t_{nuc}, H_{clock} + |C_{eff}|) \Rightarrow 1 \tag{2.34}$$

$$P_{prevented} = P_{nuc}(t_{clock}, H_{clock} - |C_{eff}|) \Rightarrow 0 \tag{2.35}$$

Hence, the nucleation time can be derived from the probability:

$$t_{nuc} = -\tau(H_{eff}) \cdot \ln(1 - P_{nuc}) \tag{2.36}$$

Experimentally, the nucleation time can be easily computed from the propagation time [3]. The propagation time is much easier to be obtained, the only missing ingredient is the domain wall velocity. The velocity can be determined by checking the displacement of the domain wall between two consecutive image (before and after the applied pulse H_{pulse} for a time t_{eff}) taken by a wide-field magneto-optical Kerr microscope (WMOKE) (see appendix A). The velocity is:

$$v_{DW}(H_{pulse}) = \frac{l_{prop}(H_{pulse})}{t_{eff}} \tag{2.37}$$

Then, the nucleation time can be determined by saturating the magnet, applying a pulse of time t_{eff} and measuring the propagating distance:

$$t_{nuc} = t_{eff} - \frac{l_{prop}}{v_{DW}(H_{pulse})} \tag{2.38}$$

In this way is possible to determine the switching time of a magnet and the corresponding clocking frequency needed, which is one of the most important figure of merit that characterized the reliability of a pNML circuit.

3 New generation of pNLM device: CoFeB/MgO thin film

In the last years, different materials showing PMA were studied to find the one more suitable for magnetic memory and logic devices. PMA was initially observed in transition metal (TM) and rare earth (RE) alloys (like TbCoFe or GdCoFe), but due to the low Curie temperature and due to the fact that the magnetic properties of RE are very sensible to oxidation, new material investigations were necessary. TMs were then exploited in multilayer structures like Co/Pt or Co/Ni where the PMA is the result of interface properties. These materials proved to be good candidates for PMA devices in term of performances, but they have drawbacks from a power consumption point of view. They show an high depinning field (H_{DEP}) and an high spin-orbit coupling which leads to very high damping constant α and results in a large threshold current (J_C) for domain wall motion ([13]). So, it was necessary to find a new structure that links the possibility to store information and do logic operations with high performance, but that also requiring low energy. Ta/CoFeB/MgO stack seems to fulfill all the desired characteristics thanks to its high anisotropy and low damping.

3.1 CoFeB/MgO interface

Li et al. demonstrated that the origin and the strength of PMA, in Ta/CoFeB/MgO/Ta structure, is linked with the nature of the CoFeB/MgO interface and with the thickness of the magnetic layer. In particular PMA arises from local lattice change and atom bonding of the TMs at the interface. Microstructural studies ([10]) show that during an annealing process of the structure, the magnetic layer starts to move from an amorphous to a crystalline state. This is associated with the onset of B diffusion which leads to the formation of a cubic crystal structure of CoFe. If the thickness of the CoFeB film is low (between 1-1.3 nm), this crystallization is not homogeneous, but it results in a partially crystallized structures, especially in the proximity of the CoFeB/MgO interface. The lattice mismatched generates strains and distortions which introduces anisotropy. More the thickness of the magnetic film increases, more relaxation, through the generation of dislocations, is introduced, reducing the anisotropy. This broken symmetry at the interface develops a crystal field effect which can introduce PMA by modifying the local band structure via spin-orbit coupling. Spin-orbit coupling leads to a decrease in the degeneracy in the TM d-orbitals and to the formation of Fe(Co) 3d - O 2p orbitals hybridization. Peng S. suggested that also the interface seed layer/CofeB plays a role in introducing PMA, again through the hybridization of both d and p orbitals by spin orbit coupling.

3.2 Sample fabrication

Stack deposition

The Ta/CoFeB/MgO/Ta stack fabricated in this work is deposited via RF magnetron sputtering at room temperature. The sample is deposited on a Si wafer (1 cm x 1 cm) with SiO_2 (100 nm thick) thermally grow on top for electrical insulation. After an hot-plate annealing to remove water particles from the surface, the Si/SiO_2 sample is introduced in the main deposition chamber. A further cleaning is done by UV radiation and ions gun in order to remove all the unwanted particles in the chamber and reach the right working pressure ($\sim 1 \cdot 10^{-6} - 1 \cdot 10^{-7} bar$). In particular, the stack is made with a $Co_{20}Fe_{60}B_{20}$ alloy. The nominal thicknesses is Ta(2)/CoFeB(1.1)/MgO(2)/Ta(3) (numbers given in nm). The plasma is generated by Ar and each material is sputtered with a working pressure of 4 μbar, exception made for the MgO layer (1 μbar) as shown in table 3.1.

Layer	**Target**	**Power** [W]	**Thickness** [nm]	**Duration** [s]	**Pressure** [μbar]
Adhesion/Seed	Ta	40	2	43.7	4
Magnetic	CoFeB	40	1.1	39.4	4
Oxide	MgO	40	2	300	1
Capping	Ta	40	3	65.6	4

Table 3.1: *Sputtering parameters*

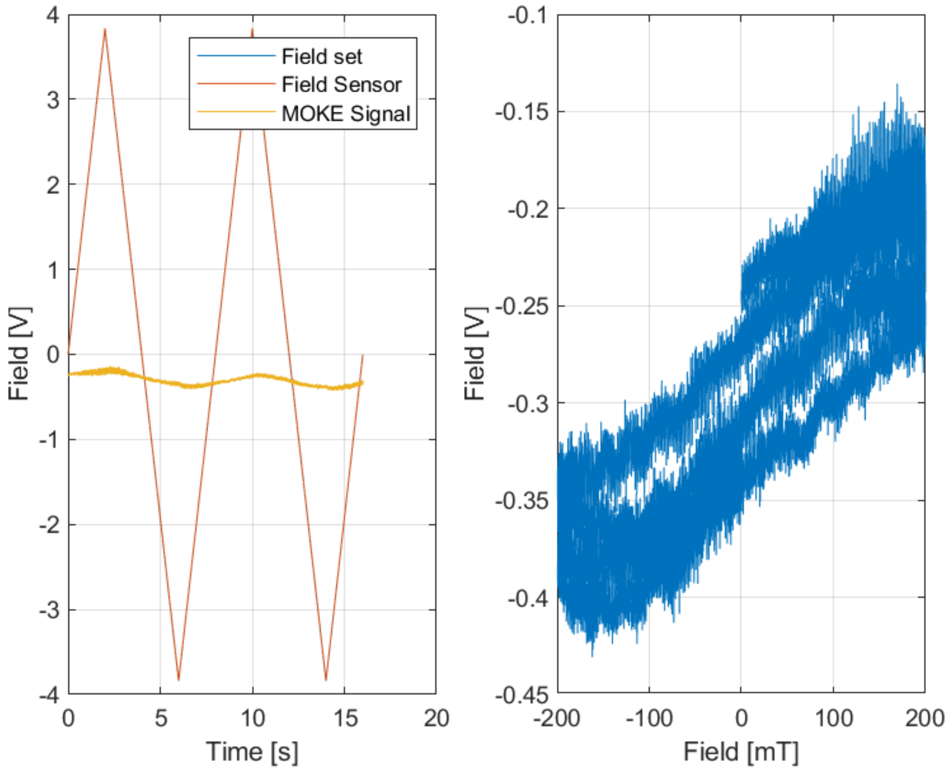

Figure 3.1: *Laser MOKE image: as deposited state. The image on the left represents the output signal of the MOKE and the magnetic field measured by the sensor over the time. On the left instead, the hysteresis.*

Ta is chosen as seed layer for different reasons:

- To minimized the roughness
- Because is a good getter of boron (B)
- To improve the PMA (as demonstrated by Peng S.)

The capping layer instead is used to protect the sample from oxidation, which can ruin the magnetic properties reducing the PMA.
After the sputtering, the magnetic properties of the sample are checked via Laser-scanning MOKE (see appendix A). The measurement result is shown in figure 3.1 The right plot shows the measured hysteresis, computed with an out-of-plane field ranging between -200 mT and 200 mT. The signal is very noisy, but it is clear that there is not a remanent state and consequently, PMA. To induce and out-of-plane magnetization, the sample needs a thermal annealing process.

Thermal annealing

From the study of Meng et al. it is shown that, depending on the thickness of the magnetic layer, there is a temperature window in which the PMA can increase. In this range, the annealing promotes the boron diffusion towards the seed layer and the onset of the crystallization of CoFe, turning the easy axis from in-plane to out-of-plane. For too high temperature, the PMA strength starts to be reduced. This can be due to a degradation of the hybridization of the Fe 3d and O 2p orbital and to the onset of the diffusion of Ta in the CoFeB ([15]). In particular, Miyakawa et al. demonstrated that the drop in the PMA starts to occur only when the Ta atoms reach the CoFeB/MgO interface, reducing $K_{interface}$.
In this work, the annealing is done in a N_2 controlled atmosphere at 275°C, for 5 minutes.

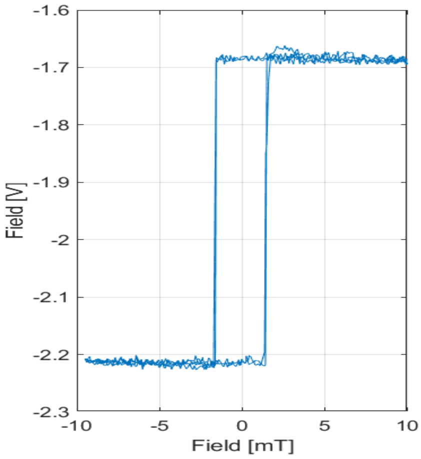

(a)

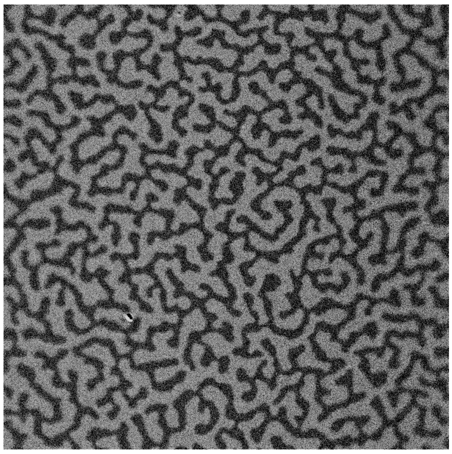

(b)

Figure 3.2: After annealing: a) Hysteresis measured by the LMOKE b) Magnetic domains imaged by the WMOKE (50x objective).

Fig.3.2 shows the sample hysteresis after annealing. The presence of an hysteresis means that, after the annealing step, the structure developed PMA. From this measure, the coercivity (H_C) is found to be $\sim 1.5mT$. The width of the hysteresis is related to the effective anisotropy energy. The effective anisotropy term keeps into account all the anisotropy contributions that favour both the out-of-plane and in-plane magnetization. But a small area is an hint that or the developed PMA is not too strong, or that the demagnetizing contribution, and so, the saturation magnetization (M_S), is quite high. Exploiting the wide-field MOKE (see appendix A), is possible to image the magnetic domains, as shown by Fig.3.2. To give an idea of the size of the magnetic domains, the image is taken with a 50x objective, which means that each side of the image is $\sim 83\mu m$. Found the wanted magnetic properties with this sample, the next step will be to pattern nanostructures on it and perform a study on their switching behaviour.

4 Engineered domain nucleation

The goal of this work is to prove the possibility to perform basic logic operation with Ta/CoFeB/MgO/Ta stack. To do so, it is necessary to have control over the domain nucleation in the magnet which acts as output gate in the logic device. After the fabrication process, the magnets show an inhomogeneous anisotropy distribution due to an unavoidable presence of defects. In this conditions, the nucleation of a new domain will occur in random spots where the local anisotropy is lower (generally close to the edges, where the amount of defects is higher). This mechanism is known as domain nucleation via coherent rotation, well described by the Stoner-Wohlfarth model ([23]). It is necessary a different nucleation mechanism, which can be controlled and which can dominate the magnetization switch of the magnet. Nucleation by depinning is an alternative, the basic principle is the nucleation of new domain in a precise region in which the anisotropy is artificially reduced. Then, to propagate in the whole material, the domain has to overcome the anisotropy gradient created between the artificial nucleation center (ANC) and the rest of the magnet. Focused ion beam irradiation is the key to reach our goal (see appendix A for more information about the FIB system). A study of Mendisch et al. demonstrated that by means of collisions between the ions and the atoms of the sample, it is possible to rearrange the sample crystallographic structure, modifying its magnetic properties. In particular, two different irradiation steps are generally needed. The first, called *areal irradiation*, is a global irradiation to obtain an uniform distribution of anisotropy and increase its value over the whole magnet, while the second is a local irradiation, with an higher dose, to create the ANC. In this section a study over different ions doses for both the steps is performed. The aim is to find the right doses that allow to control over the nucleation phenomenon. Moreover, also the position and the geometry of the artificial nucleation center will be investigated through micromagnetic simulations, in order to optimize the reversal magnetization process.

4.1 Structures patterning

The structures under test are six wires with different widths, from 700 nm to 450 nm (step of 50 nm), with a length of 10 μm (Fig.4.1(a)). The patterning process is summarized in the following steps:

- FIB lithography
- Hard mask evaporation
- Lift off
- Ion beam etching

First of all, the PMMA resist ($\sim 35nm$) is spin coated on the sample and then it is illuminated by FIB, with a Ga^+ ions dose $\sim 3.8 \cdot 10^{12} \frac{ions}{cm^2}$. After the irradiation the resist is developed, obtaining the negative of the mask layout (being the PMMA a positive resist). As hard mask for etching, a thin layer of Ti ($\sim$ 6.5 nm) is deposited over the whole structure and then, by a lift-off process, all the resist and consequently the Ti on top of it, are removed. By Ar^+ ions beam etching, all the parts not covered by the Ti mask are etched, obtaining the mask layout.

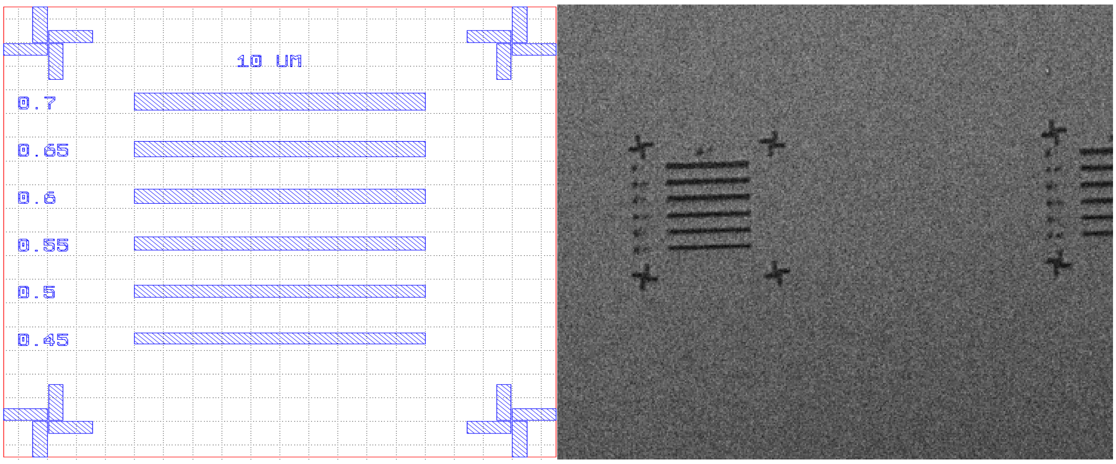

(a) (b)

Figure 4.1: *a) CAD model of a box containing the test structures to pattern for the irradiation study b) WMOKE image of the patterned test wires (50x objective).*

The sample contains different boxes with the same structures inside. Each of these box will be irradiated with a different ion doses in the next irradiation studies.

In this patterning process, not only wires are fabricated, but also the planar inverters on which we will discuss later.

4.2 Areal irradiation study

The *areal irradiation* is a global irradiation with the aim of uniforming the anisotropy of the magnet [12]. The idea behind this process is to modify the stechiometry of the magnet, through a quite low ion dose. The main effect is an increase in the switching field of the structure by few mT. This increment allows also to have an higher switching field difference between input and output, which is fundamental to perform logic operations. This result comes from the work of Mendisch et al., where it was found an interesting trend of the coercivity with respect to the FIB irradiation dose. As shown in the graph on the right in fig.4.2, increasing the dose value, the coercivity undergoes an increment for the lowest doses, reaches a maximum and then starts to decrease to zero (in-plane magnetization condition). But the ion doses are not fixed, they vary sample by sample. They strongly depends on the physical characteristics of the structures after the fabrication process, like the amount of defects. The aim of this section is to study different ion doses in order to find the one that maximizes the switching field of the wires.

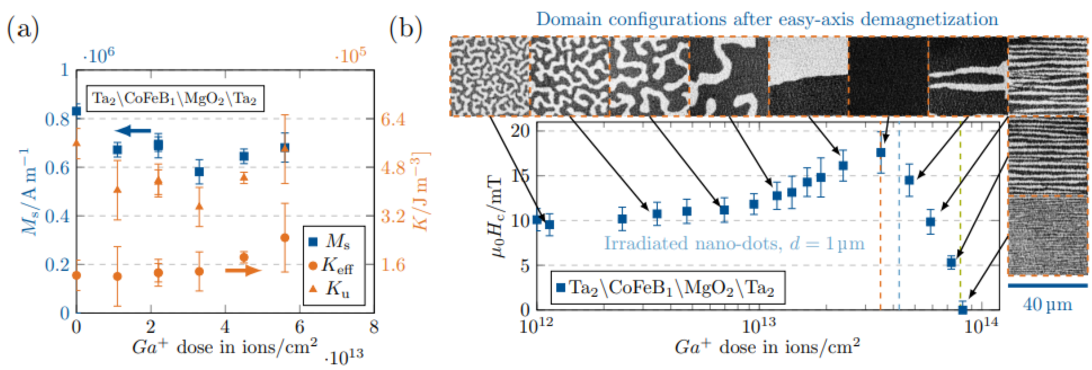

Figure 4.2: *Ga^+ dose dependent evolution of the saturation magnetization M_s and coercivity H_c (image taken from [11]).*

4.2.1 Methodology

The experiment is carried on measuring by WMOKE the switching field of the wires before and after the irradiation. The measurement is done by generating a train of pulses with an increasing field value. For each field value, five pulses are generated in order to include statistics. Before each excitation pulse, a saturation pulse with opposite value is applied to induce a reset state. To check the switching of the magnets, an image before and after each excitation pulse is taken and the corresponding differential image is analyzed. The differential image is used to maximize the contrast and to highlight the switching event. This procedure is repeated before and after the FIB irradiation, where each box of wires is illuminated with a different ion dose.

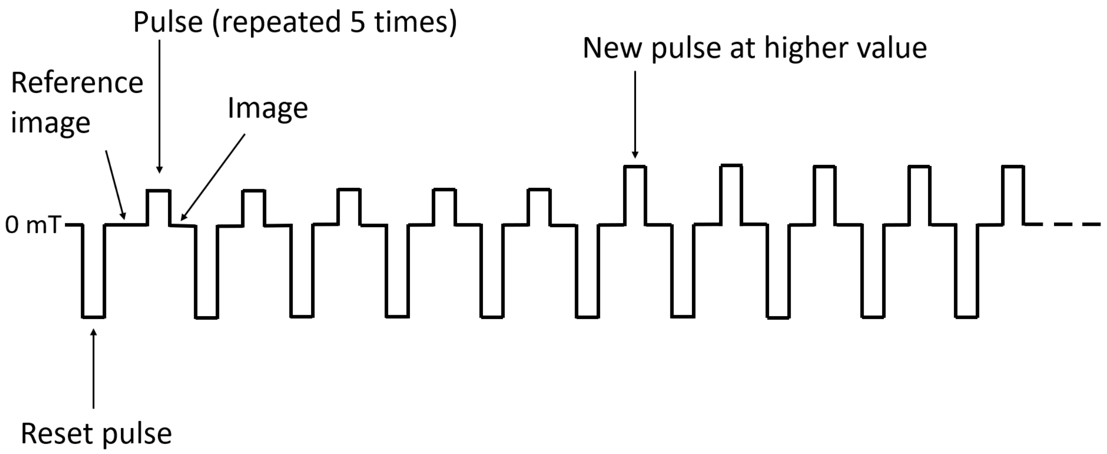

Figure 4.3: *Sketch of the train of pulses implemented for the switching field measurement by WMOKE.*

4.2.2 Results

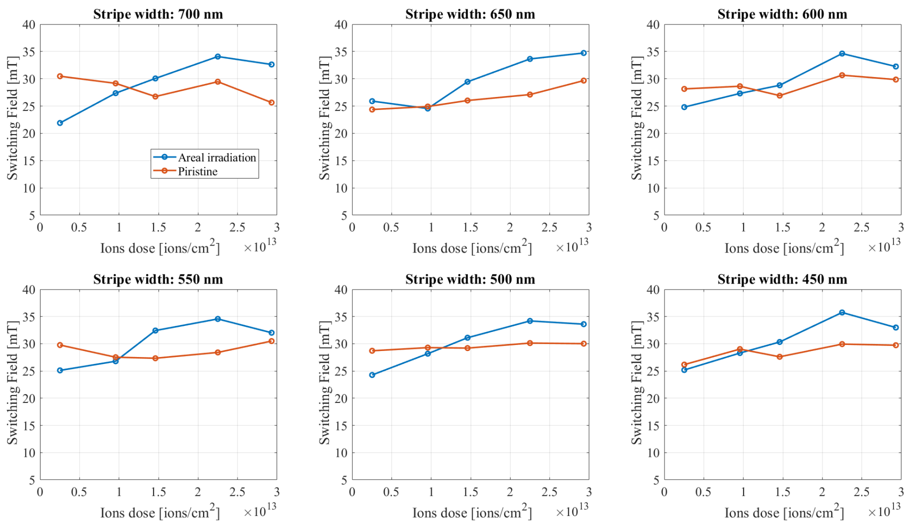

Figure 4.4: *Areal irradiation results: switching field comparison before (red curve) and after background irradiation (blue curve). Each point of the plots is referred to a wire belonging to a certain box illuminated with the corresponding dose (five boxes, five different ions doses).*

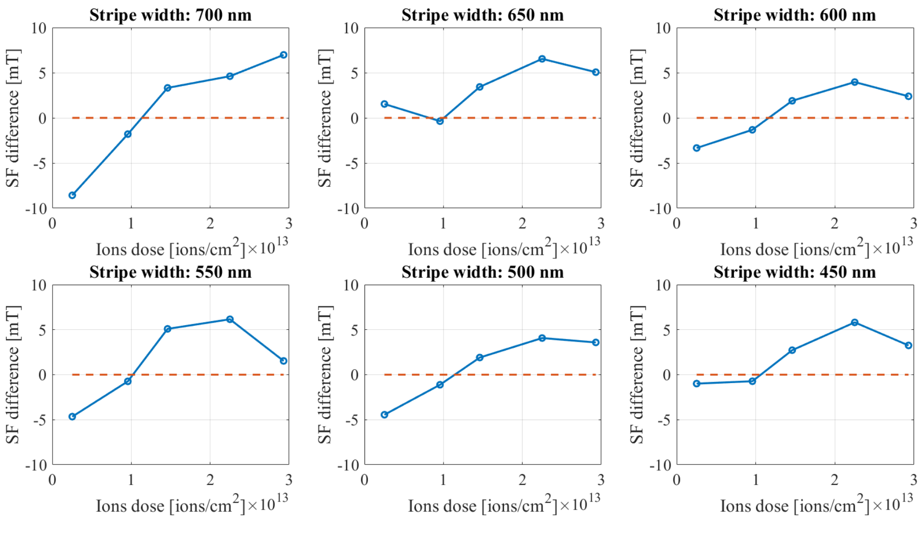

Figure 4.5: *Areal irradiation results: switching field difference (after irradiation - before irradiation). The red-dashed line is a reference to highlight the zero value.*

Fig.4.4 shows the comparison between the switching field of the wire in the pristine state (red curve) and after the FIB illumination (blue curve). Each plot is referred to a wire with a certain width. In this study five boxes patterned with the same mask are analyzed. Every box has been illuminated with a different dose, which means five different ions doses (each point of a plot is referred to a wire belonging to a specific box which is irradiated with a specific ions dose). To better appreciate the results, fig.4.5 presents the switching field difference of the stripes after the irradiation and before the irradiation. We are interested in the region in which the switching field difference is positive, i.e the ion doses for which the switching field is increased. Except for the first plot (wire of width of 700 nm), all the other structures show the same trend. The difference is negative for the lower dose. Increasing the dose it becomes positive, it reaches a maximum and then decreases. The highest switching field difference is found for a global irradiation of $2.25 \cdot 10^{13} \frac{ions}{cm^2}$ for five structures over six. This value differs quite a lot from the results found by Mendisch et al. (which is $\sim 3.5 \cdot 10^{13} \frac{ions}{cm^2}$), even if the stacks composition is the same. The found value will be used for the areal irradiation in the next studies. The increment in the switching field is considered to be related to a rise in the effective anisotropy (K_{eff}). What is not clear is if this variation is due to an enhancement of the uniaxial anisotropy (K_u), a reduction of the saturation magnetization (M_s), or both the effect together, after the FIB induced crystallographic rearrangement. Different studies present in literature can help to better understand what happens. Mendisch et al. demonstrated a reduction in the magnetization saturation after FIB irradiation with Ga^+ ions. This behaviour is attributed to an intermix of Ta within the CoFeB layer. Tantalum is known to have a large magnetic dead layer, and so, the resulting CoFeTa alloy is characterized by a lower magnetization with respect to CoFe. The same observations were done by Devolder et al. (even if they worked with He^+ ions, lighter than Ga^+).

4.3 ANC study

Although the reduction of the magnetization, the behaviour of the switching field found in the previous study is not monotonic, but after a certain value of ion dose, it starts to drop. This can be due to the fact that, when the amount of atom-ion collisions becomes higher, an higher intermix of atoms occurs. This intermix can ruin the CoFeB/MgO interface, strongly affecting the anisotropy. The creation of an ANC exploits this effect. A local irradiation with a quite high dose generates a region in the magnet in which the effective anisotropy (K_{eff}) is locally reduced and consequently the field needed to nucleate a new domain, decreasing the switching field of the whole magnet. In this way, the nucleation will occur in a well defined region of the sample, inactivating all the inherent random nucleation spots. Logic operations are based on the coupling between the inputs and the output, which can prevent or support the magnetization reversal of the output [3]. Hence, it is fundamental to have control over the position in which the nucleation of the opposite domain occurs. This section investigates the effect of the presence of an ANC on the wires, with the aim to strongly reduce their switching fields. In particular, the stripes are firstly globally irradiated (*areal irradiation)* with the dose found in the previous experiment, and then, locally irradiated to study different ion doses for the ANC.

4.3.1 Micromagnetic simulations

Before proceeding with the experiment, micromagnetic simulations are used to characterize the most efficient layout in terms of ANC geometry and position. The simulations are performed with the GPU accelerated package software Mumax3 ([26]). The simulated structure is a wire with length of 400 nm, width of 80 nm and a thickness of 1 nm (fig.4.6). The magnetic properties are listed in the next table.

Parameter	Value	Unit of measure
M_s	$8.3 \cdot 10^5$	$\frac{A}{m}$
Ku_{film}	$5.6 \cdot 10^5$	$\frac{J}{m^3}$
Ku_{ANC}	$0.7 \cdot Ku_{film}$	$\frac{J}{m^3}$
α	0.015	-
A_{ex}	$2 \cdot 10^{-11}$	$\frac{J}{m}$

Table 4.1: *Magnetic parameters implemented in the simulations*

The value of the magnetization saturation (M_s) and uniaxial anisotropy constant (Ku_{film}) are taken from the study of Riente et al. and are measured values from a sample similar to the one fabricated in this work. The damping constant (α) and the exchange stiffness (A_{ex}) instead, are taken from the literature ([24]). The discretization of the sample is 2.5 nm x 2.5 nm x 1 nm. The first parts of the simulations regards the position of the ANC. Two different layout are simulated, the first, with the ANC in the center of the wire, the second with the ANC in contact with the uppermost border (as shown in Fig.4.6).

(a) (b) (c)

Figure 4.6: *Simulated structures: a) squared ANC (50 nm side) in the center, b) squared ANC (50 nm side) at the border, c) circular ANC (56.4 nm diameter) at the border. The wire is 400 nm long, has width of 80 nm and is thick 1 nm.*

The difference in the switching behaviour is investigated through an hysteresis analysis of the two layouts. These simulations are statics and the external field is varied in three steps. From 0 mT to 200 mT, then from 200 mT to -200 mT and finally from -200 mT to 200 mT. The field step is 1 mT and the z-component of the magnetization vector of the whole wire is acquired at each field value. Fig.4.7 shows the comparison of the computed hysteresis. With the ANC at the border, the switching occurs several mT lower ($\sim 34mT$ in this analysis) than the case in the center. This, although the maximum value of demagnetizing field which helps the magnetization reversal, should be in the center of a magnet. The reason could be found in the fact that at the border, the magnetic moments tend to naturally turn faster at the edges. It is worth to say that these very high values of coercivity ($H_{c-border} = 120mT$ and $H_{c-center} = 154mT$) are obtained not keeping into account in the simulation the thermal effects, the presence of grains and possible material defects.

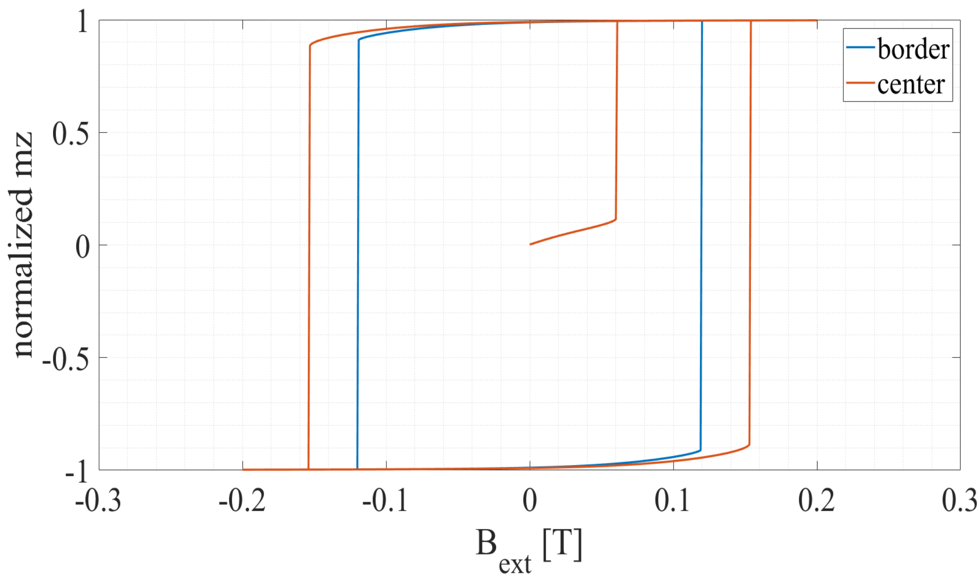

Figure 4.7: *Hysteresis comparison of a wire with the ANC placed at the border (blue curve) and at the center (red curve). Structures represented in fig.4.6* (a) and (b)

The other question investigated in this simulative study is if the shape of the ANC has an impact on the switching behaviour of the magnet. Two structure are simulated, one with a squared ANC (50 nm x 50 nm) and the other with a circular ANC, with the same volume of the first (diameter = 56.4 nm). From the hysteresis in Fig.4.8 a small difference of 2 mT is present between the two cases. In particular, the ANC with square shape allows to reach lower switching fields.

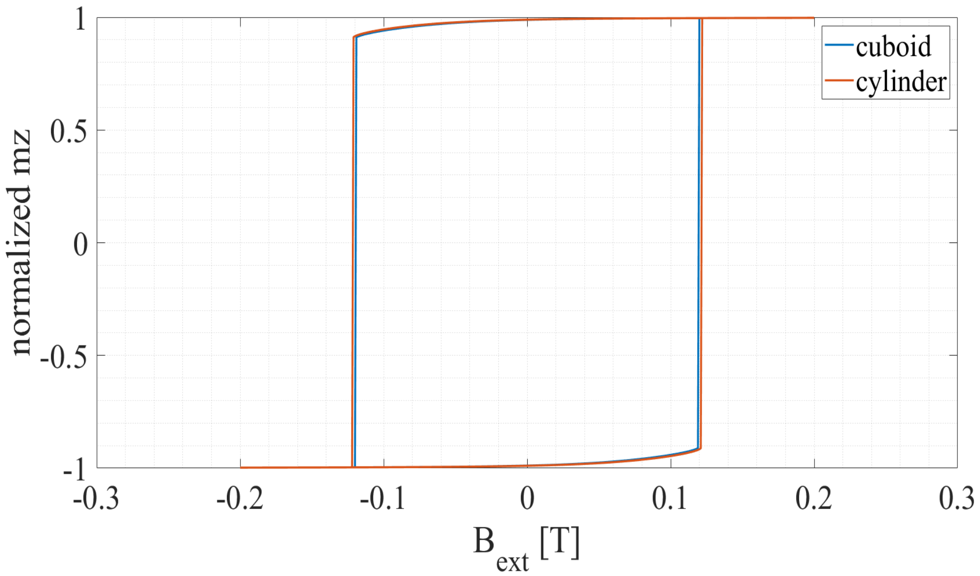

Figure 4.8: *Hysteresis in case of squared and circular ANC placed at the border. The simulated structures are shown in fig.4.6 (b) and (c).*

These simulations suggest that placing a squared ANC in contact with the border of the wire (fig.4.6 (b)) can help to reduce the switching field maximizing the effect of the ANC with respect to other layouts, allowing to decrease the energy and power consumption during logic computation.
Another way to maximize the efficiency of the ANC can be found investigating on the external field applied to switch the magnetization. In all the previous simulations and real experiments, the external field was applied perpendicular to the surface structure ($B = (0{,}0, B_z)$). The aim is to check what happens to the magnetization dynamics when the external field is tilted by an angle, i.e adding x-y components in the simulation. The simulated structure is a disk of 500 nm diameter, with an ANC of 100 nm diameter in the center. The magnetic parameters are the same of the previous simulations (see table.4.1). The module of the field is keep fixed at 120 mT, while its angle with respect to the z-axis (angle θ) is varied from 0° (out of plane) to 90°(in plane). The initial magnetization configuration of the magnet is mz = -1.

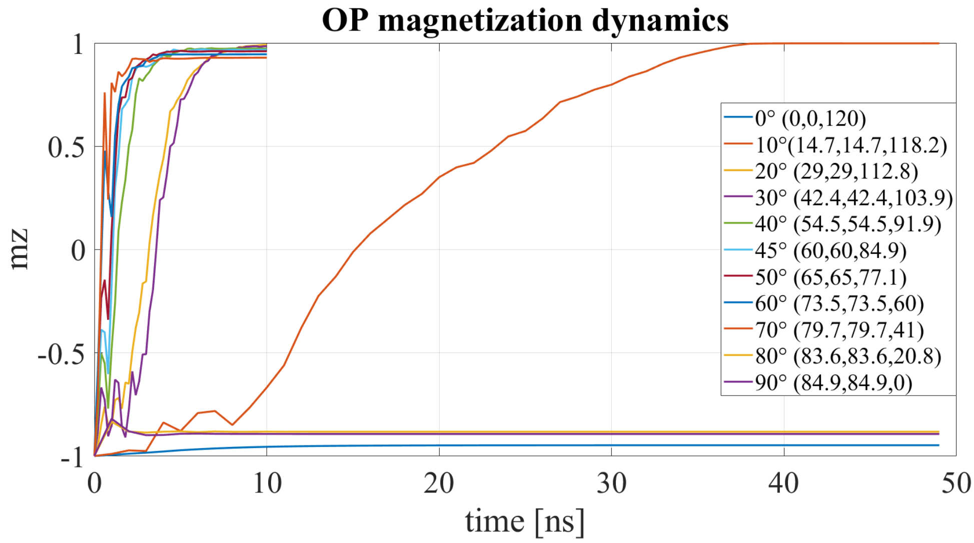

Figure 4.9: *Magnetization dynamics of the simulated disk: evolution of m_z over time under different field angles with respect the out-of-plane direction.*

Fig.4.9 shows as the switching dynamic of the whole disk evolves in time. When the applied external field is completely out of plane ($\theta = 0°$) or in plane ($\theta = 90°$) the switch doesn't occur. When instead the field starts to be tilted ($\theta = 10°$), a new domain nucleates in the ANC and propagates, leading to a complete switch of the magnetization after 38 ns. Further increasing of the angle, and so, the component along x-y, the switching time is drastically reduced down to 4 ns. This happens up to an angle $\theta = 70°$, after that, the out-of-plane component of the field is not enough to generate a new domain in the ANC and m_z remains constant to -1 (initial state). Following the simulation switching dynamics, it's clear that the presence of x-y components in the field helps the switch of the magnetization and depending on their module, seems that different propagation mechanisms take place. Higher are the module of B_x and B_y, faster is the nucleation and a radial and more uniform propagation of the new domain from the ANC to the whole magnet occurs. This is translated in a faster switching. If there aren't any x-y components of the field or the angle is lower than 20°, the nucleation is slower and the propagation is not uniform. The domain starts trying to reach firstly the edge of the sample in a random region of the border and then it expands in the whole magnet. Fig. 4.10 and Fig. 4.11 compare the switching dynamics under an external field with angle ($\theta = 10°$) and ($\theta = 70°$).

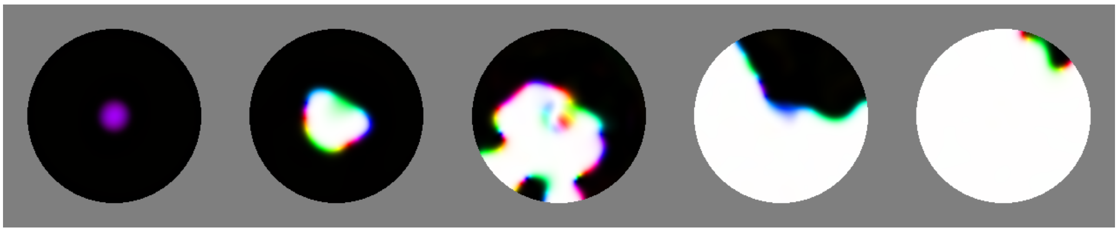

(a) 3 ns (b) 9 ns (c) 13 ns (d) 20 ns (e) 35 ns

Figure 4.10: *Simulated switching dynamics, $\theta = 10°$. Sequence of images which show how the switching process of the magnet evolves over time.*

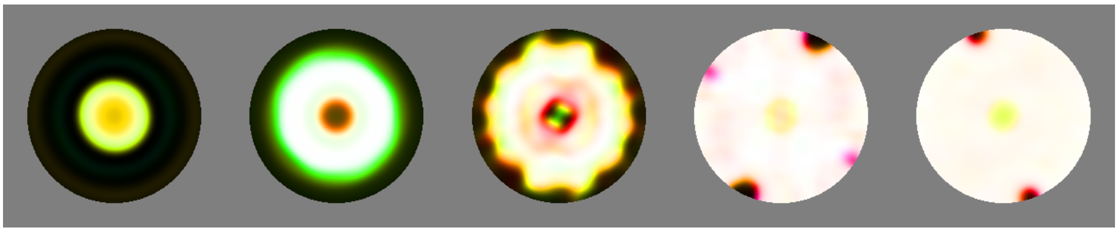

(a) 0.2 ns (b) 0.4 ns (c) 0.8 ns (d) 2 ns (e) 3.2 ns

Figure 4.11: *Switching dynamics, $\theta = 70°$.* Sequence of images which show how the switching process evolves over time.

As shown above, exploiting a titled bias field can allow to reach computing frequencies up to one order of magnitude higher, or to decrease the amount of field needed to perform the logic operations, saving energy. The only problem is how to physically implement such a tilted external field. From this result, another consideration can be made for what concern the best position for the ANC. The region of the magnet in which the demagnetizing field presents its highest value in module is the center. The demagnetizing field tends to switch naturally the magnet state counteracting the magnetization vector. For this reason, to place the ANC in the center should be the best layout to maximize the ANC efficiency. But from the previous simulation (fig.4.7) it was found the opposite; i.e, to place the ANC at the edge results in a lower required switching energy. This can be also explained exploiting the results of this last simulation (fig.4.9). In fact, in the middle of the magnet, the stray field is completely in-plane ($B = (B_x, B_y, 0)$) and it has not the z-components, while at the border of the sample it presents all the components ($B = (B'_x, B'_y, B'_z)$), and this can allow a faster and more probable nucleation and switching event, maximizing the efficiency of the ANC.

4.3.2 Experimental results

From the simulations, all the geometrical and layout information to maximize the ANC efficiency are obtained. This information are now exploited in this section to perform the real experiment. After an areal irradiation with dose equal to $2.25 \cdot 10^{13} \frac{ions}{cm^2}$, the artificial nucleation centers are created. The ANCs are squares placed at the left border of the wires. The size of the ANC depends on the width of the wires, its side is equal to half of the wire width.

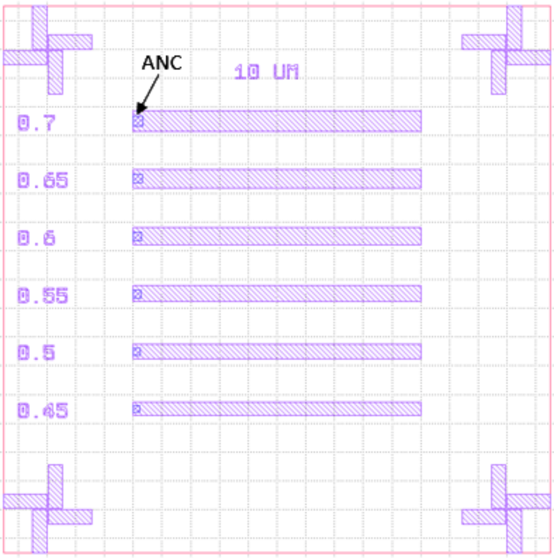

Figure 4.12: *CAD model for the ANC irradiation*

The results are obtained with the same measurement set up as in the areal irradiation study, and they are presented in the same way. Fig.4.13 shows the comparison of the wires switching field in their pristine state (red curve) and after the double illumination step (blue curve). To better understand which dose reduces the most the switching field, the second figure (fig.4.14) presents the effect of the ANC plotting the difference of the switching field of the wires before and after the irradiation.

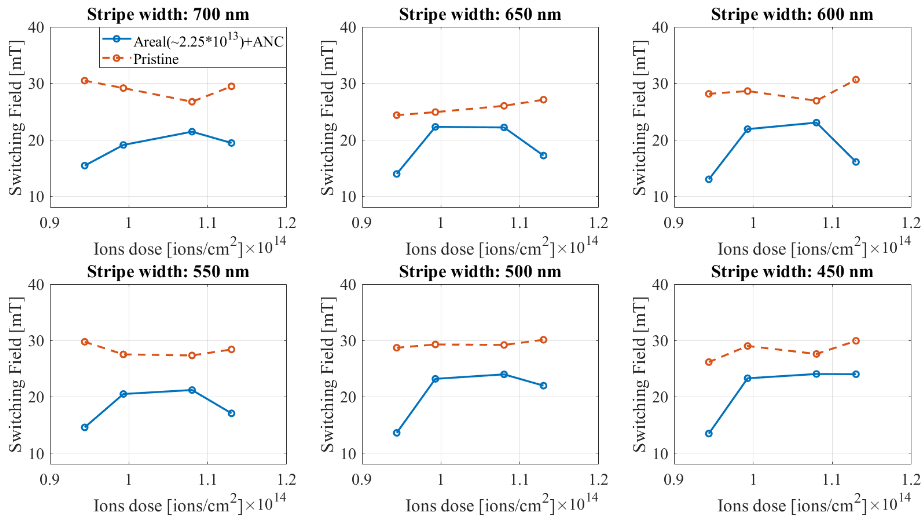

Figure 4.13: *ANC study results: switching field comparison before (red curve) and after irradiation (blue curve). The irradiation consists in the global areal irradiation (fixed at* $2.25 \cdot 10^{13} \frac{ions}{cm^2}$*) plus the local irradiation for the ANC creation. The values on the x-axis are referred to the cumulative ions dose in the ANC region.*

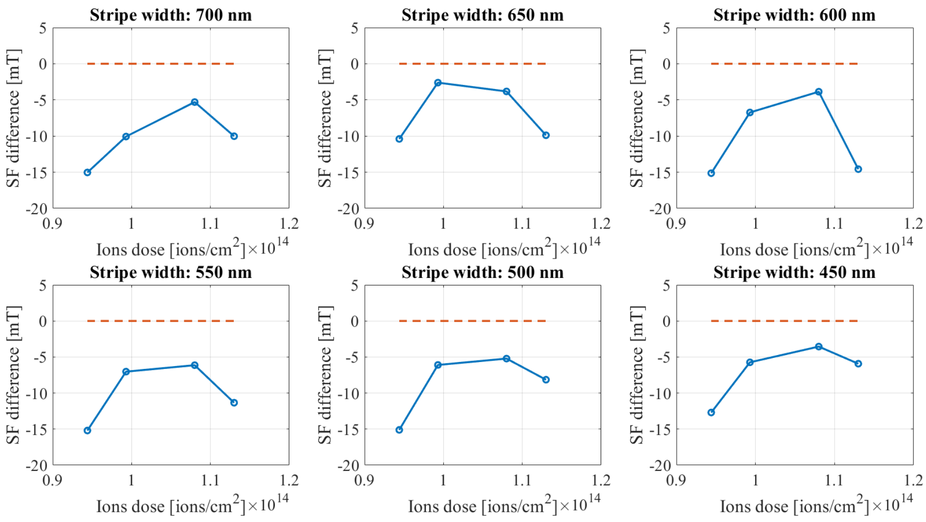

Figure 4.14: *ANC study results: switching field difference (after irradiation - before irradiation). The red dashed curve is a reference which represents the zero value.*

All the graphs in Fig.4.14 show a particular trend. The lowest ion dose is the one that decreases the most the switching field. Increasing the amount of ions, the switching field difference is reduced in modulus, reaches a minimum and then increases again. It is worth to say that probably, this is not the best range of doses for the ANC creation. It is expected that lower doses can reach even higher difference in the switching behaviour. The dose range used in this study is probably too high, and the efficiency of the ANC starts to degrade. Anyway, these results are enough for our final goal. They demonstrate that, with FIB irradiation, it is possible to tune the magnetic properties in such a way to have different switching behaviour between input and output, and to have control over the nucleation mechanism. These ingredients are fundamental to perform logic operations. What is still missing, to prove really the possibility to do logic with magnets, is the presence of coupling between input and output. This, will be investigated in the next section.

5 2D Logic device

The basic logic device used in pNML is the inverter. It consists in two nanomagnets antiferromagnetically coupled, with the aim to invert the information. Being coupled antiferromagnetically, the coupling field generated by the input supports the switch of the output in the opposite magnetization state, inverting the signal encoded in the input. At the same time, this coupling field prevents the switch of the output in the same magnetization state of the input. In this section, different co-planar inverter structures are investigated with the aim to measure the presence of coupling and its strength, in order to validate the possibility to perform the logic. The strength of the coupling field depends on different parameters. On magnetic parameters, as the magnetization saturation (M_s) of the input, but also on spatial parameters, like how the input structure is geometrically arranged around the ANC and how much distant it is from the ANC. The devices under test are fabricated by FIB lithography as described in chapter 4. Micromagnetic simulations are exploited to check the presence of the coupling and the possibility to perform the inversion operation. The simulated structure is similar to the real patterned one, the gap between input and output is 100 nm and the ANC is a square of 50 nm side place in contact with the leftmost border of the output; a wire of 100 nm width. The magnetic parameter are the same as before, with the difference that, in this case, the temperature and the presence of grains are taken into account.

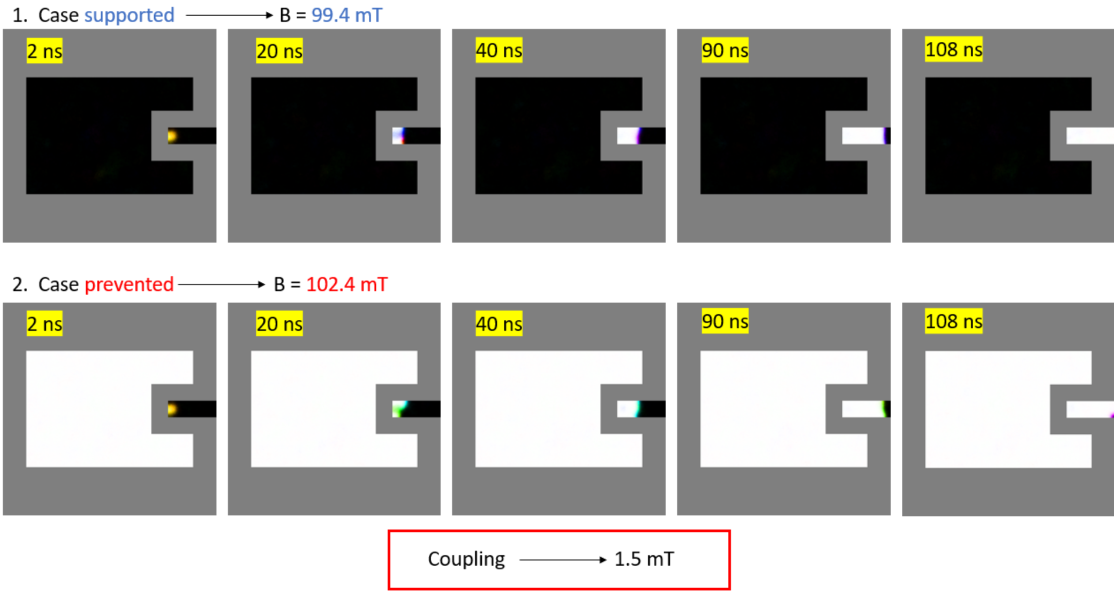

Figure 5.1: *Micromagnetic simulation of an inverter in the case in which the inversion is supported (upper row) and prevented (bottom row). The magnetic parameters of the structure are listed in table 4.1. The input has a fork-like structure to surround the ANC and maximize the efficiency of the coupling. The dimensions are 0.7 μm x 1 μm, the gap is 100 nm as the width of the output and the ANC is a square of 50 nm side placed in contact with the left border of the output. In this simulation, temperature and grains are taken into account.*

The output initial magnetization state is pointing downward ($m_z = -1$) and a positive field is applied along z, to switch the output magnetic state. In the supported case, the initial situation is the one in which input and output have the same magnetization, and due to the antiferromagnetic coupling, the output switch is helped by the stray field generated by the input. This allows to invert the information encoded in the input magnetization. In the prevented case instead, input and output have the opposite magnetization and an inversion of the input signal is already present in the initial state. So, a switch of the output should be counteracted by the stray field of the input. The coupling can be easily computed finding the lowest field that allows the switch of the output in the two cases. From this simulation, the lowest switching field in the supported case is 99.4 mT, while in the prevented case is 102.4 mT. The presence of a difference in values means that the coupling exists, and having an higher field in the prevented case means that is correct. The coupling field is computed as:

$$C = \frac{Hp - Hs}{2} = \frac{102.4 - 99.4}{2} = 1.5mT \tag{5.1}$$

Fig. 5.2 (a) shows the mask file used in the FIB lithography of a box containing the inverters. The numbers on the right refer to the dimension of the gap between input and output, for the inverters in the corresponding row, while the ones on the top refer to the width of the last part of the output, for the inverters in the corresponding column. Fig. 5.2 (b) shows a zoom of one inverter to check the common dimensions among all the structures, as the size of the input and the width of the initial part of the output, which should be 100 nm in width. This region will host the ANC. The ANC is a square of 50 nm side which should be placed in contact with the left border. The conditional is used because, due to unavoidable misalignment inaccuracies, hit with FIB exactly a region of 100 nm, is not an easy task. Hence, it is not obvious that we will be able to place the ANC in the precise designed position. Fig. 5.3 shows the real patterned box imaged by the WMOKE (figure (a)) and a single inverter imaged by AFM (figure (b)). The AFM is used also the measure the structures dimensions after the lithography process. Due to resolution issues, the patterned structures present higher dimension in the smallest features with respect the designed layout. For example, the inverter in fig.5.3 (b) should have a nominal gap of 100 nm, but from the AFM measure it is estimated to be $\sim 150nm$.

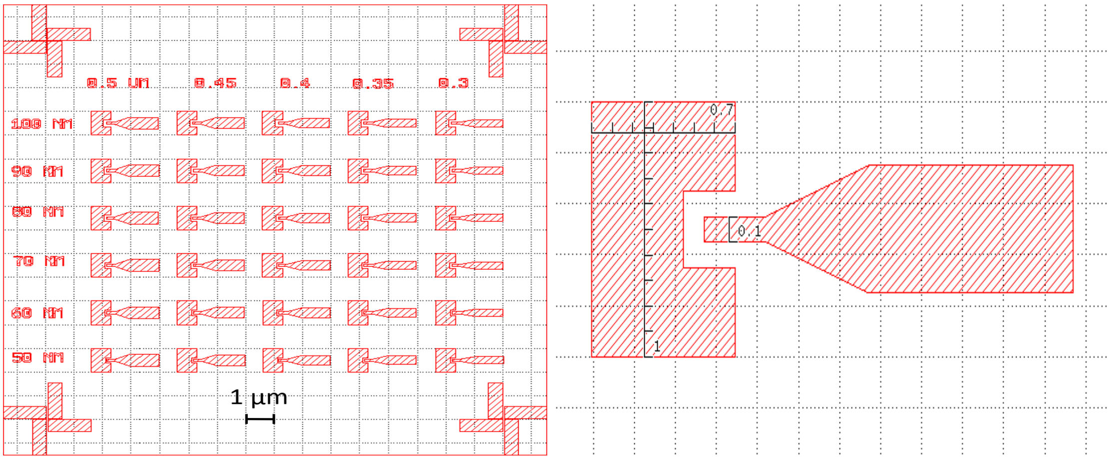

(a) (b)

Figure 5.2: *CAD model for the inverters FIB lithography process: a) Complete FIB lithography mask, b) Zoom of an inverter showing the common size in µm. The structure on the left is the input, the one on the right the output. The input has a length of 700 nm and a width of 1 µm, while the total length of the output is 1.8 µm and the width of the narrower region is 100 nm.*

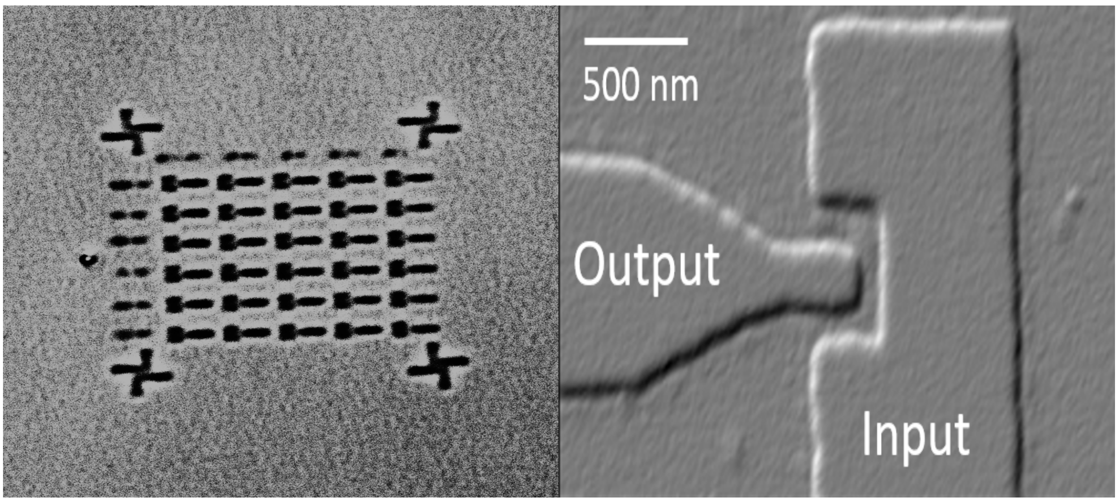

(a) (b)

Figure 5.3: *a) WMOKE (50x objective) image of a FIB lithography patterned box containing 30 inverters, b) AFM image of an inverter with nominal gap of 100 nm (real gap ∼ 150 nm)*

The first step consists in to modify the magnetic properties of input and output by FIB irradiation. All the required information come from the previous studies. Both input and output undergo to an areal irradiation and then, the ANC is created in the output. Due to misalignment in the irradiation process, only twelve inverters over thirty present the ANC correctly placed in the output. Fig.5.4 shows the evolution of the switching field of these twelve working inverters, before and after the irradiation steps (only the areal irradiation for the input and areal plus ANC creation for the output) . In particular each graph is referred to a specific inverter. Before the irradiation, the switching fields of input and output were distributed randomly, while after the tuning, there is a net difference between them. The outputs (red curves) show a drop in the switching field after the double irradiation step (areal + ANC), while the inputs (blue curve), in most of case present an increment in the switching field. The result, as expected, is a net difference in switching field, between 10 and 20 mT, with the input harder then the output.

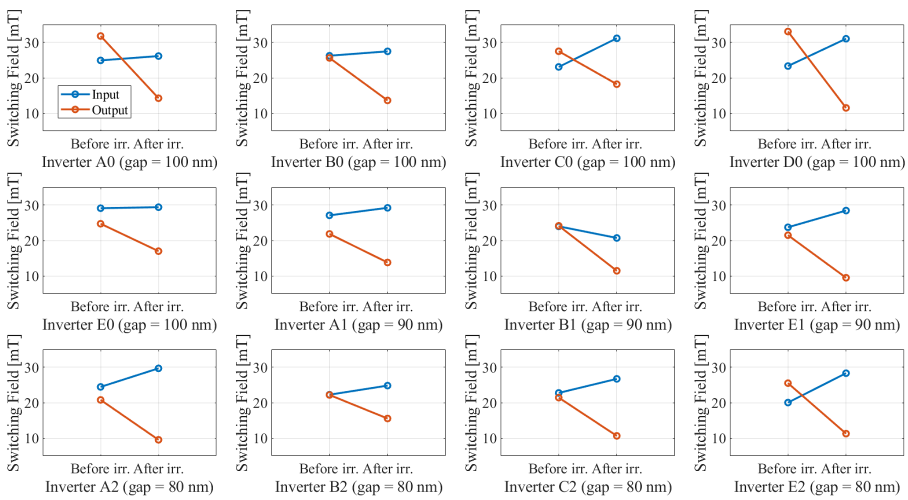

Figure 5.4: *Working inverters results: switching field behaviour of input (blue curve) and output (red curve) before and after the irradiation steps*

After being able to correctly tune the switching behaviour, the last and missing ingredient to prove the logic is the coupling. To measure it, two different measurements are required. The idea is to measure the switching field of the output in the supported case and in the prevented case, and extrapolate the coupling exploiting the formula 5.1. The measurement technique is the one already explained in section 4.2, but with some modification for the switching prevented case. In the supported case, a negative reset field is applied before each positive switching pulse, in order to have always the initial situation in which both input and output have a negative magnetization (input = -1, output = -1), and the positive switching field of the output (H_s) is obtained. In the second case instead, a first reset high enough to switch both input and output to -1 is applied. Then, to set the initial configuration (input = -1, output = +1), a positive reset field high enough to switch only the output is used. Finally, through the application of negative pulse, the output is forced again to switch to -1. In this way, the negative switching field of the output (H_p) in the prevented case is acquired. Fig.5.5 summarizes the measurement techniques.

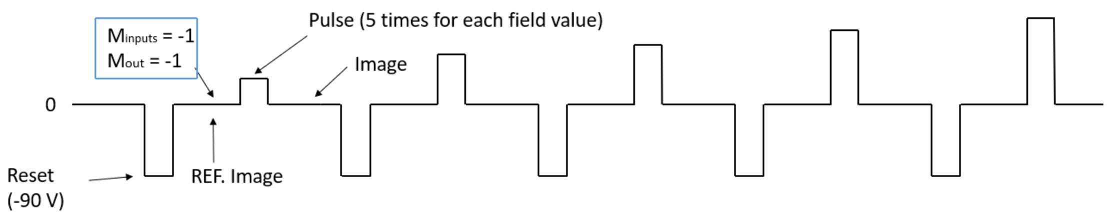

(a) Supported case

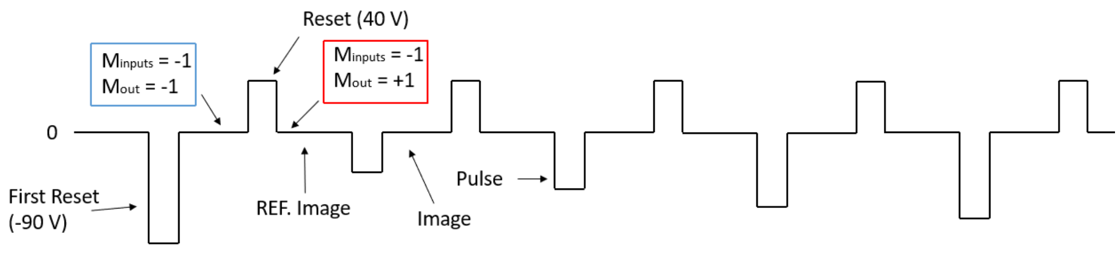

(b) Prevented case

Figure 5.5: *Coupling measurement train of pulses set up*

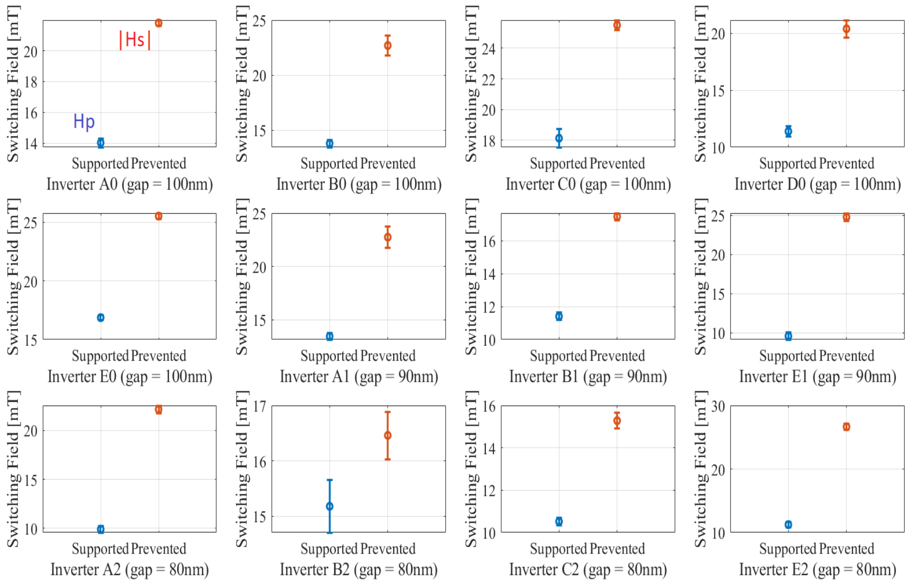

Figure 5.6: *Coupling measurement result for the twelve working inverters. In blue the measured switching field of the output in the supported configuration, while in red, the result in the prevented configuration*

Fig.5.6 shows the comparison of H_s and $|H_p|$ (in absolute value, being negative) for each of the working inverters. The coupling is computed exploiting the formula 5.1 and the results are summarized in the following table:

Inverter	**Nominal gap [nm]**	**Coupling field [mT]**
A0	100	3.9
B0	100	4.45
C0	100	3.7
D0	100	4.5
E0	100	4.3
A1	90	4.65
B1	90	3.03
E1	90	7.6
A2	80	6.1
B2	80	0.64
C2	80	2.4
E2	80	7.7

Table 5.1: *Coupling field results*

The found coupling fields differ a lot from the result of the simulation and also between them. They range from a very low value (0.64 mT) to a very high one (7.7 mT). There is not a net trend depending on the dimension on the gap. It was expected that, decreasing the gap, the coupling field would have increase in value. In the case of 100 nm gap, the values are quite stable around 4 mT, while in the other cases there is an higher variation. Probably, the main role in this oscillation is played by the low resolution when correctly placing the ANC. This because, few nm of inaccuracy can lead to a variation of coupling of few mT. In the cases of the inverters B2 and C2, the low value of coupling field (0.64 mT and 2.4 mT) is the result of a partial ANC irradiation, i.e the ANC was not completely centered in the output and so, the region sensible to the input stray field is reduced, decreasing the coupling. Anyway, although the high variability introduced by the fabrication process, Ta/CoFeB/MgO/Ta stack proves to be a good candidate for pNML. It was possible to reach very high value of coupling and modify by FIB the switching behaviour of the magnet up to 20 mT, reaching switching field value of the output lower then 10 mT. This is enough to prove the possibility to perform at least basic logic operation as an inversion with a coplanar layout. More efforts con be done to improve the field interaction and create a more reliable logic device. Both the fabrication process and the design of the magnets shape can be investigated to have a stronger and more stable dipole-coupling. To modify the shape of the gates enables to surround the output and the ANC with more magnetic material increasing the field interaction. From the fabrication point of view, higher resolution technique as EBL can allow to decrease the distance between input and output and to reduce manufacturing variability. Another option can be to completely change the layout, moving from a co-planar structure to a 3D one. This solution will be investigated in the next chapter.

6 3D Logic device

In this section it is explored the possibility to create 3D logic devices with Ta/-CoFeB/MgO/Ta stacks. This requires the fabrication and patterning of a new sample and a new irradiation study. A double stack of Ta/CoFeB/MgO/Ta, with MgO as interlayer, is deposited and patterned in order to fabricate two different kind of structures. The goal is to reproduce the simulated 3D structure (fig.6.1(b)), a double input gate which can act as a majority voter with the addition of a third virtual input (like a bias field). The idea is to use FIB lithography to create two islands in the top stack (inputs), keeping unaffected the bottom one (output) The other structure instead, is a single input gate (only one island in the top stack) that can be considered as an inverter structure thanks to the antiferromagnetic coupling with the bottom stack. As in the previous experiment of the co-planar inverter (section 5), after the fabrication and characterization, the structures are irradiated and a ANC is created in the output to improve the sensibility to the dipole-coupling. Going toward three dimensional layout can offer different improvements ([20], [18]). First of all, move the input and the output on different layers gives the possibility to reduce the effective dimension of the device. This allows to increase the number of logic gate per chip and so, the computing capability. Moreover, Riente et al. demonstrates how a 3D stacked layout can reach much higher coupling strength in the region of the output with respect to its complementary co-planar layout. This is proved by micromagnetic simulations in which the coupling field of the two layouts are compared.

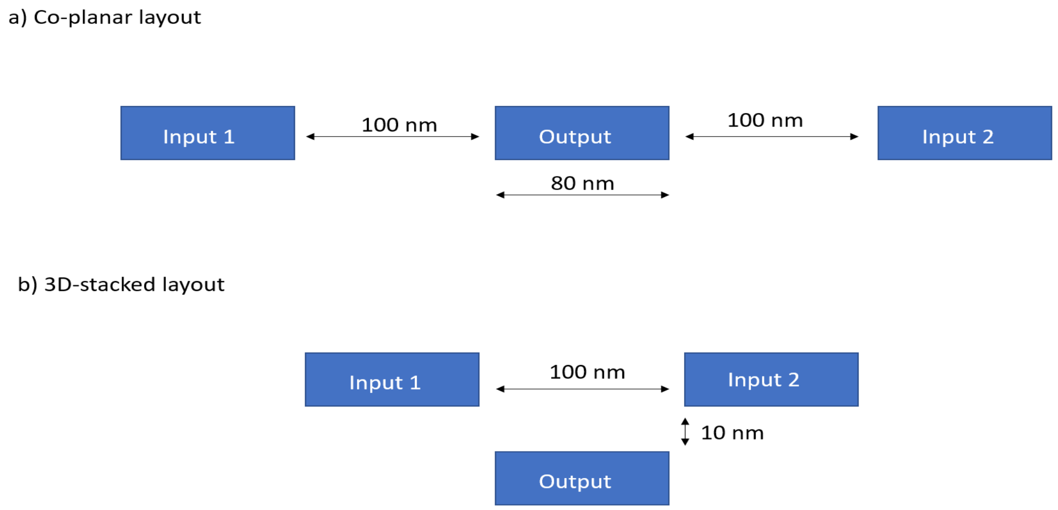

Figure 6.1: *Simulated structures: the simulated structures are wires of 400 nm length, width of 80 nm and a thickness of 1 nm. The grid dimension is 256 x 256 x 1 and the size of a single cell is 2.5 nm x 2.5 nm x 1 nm.*

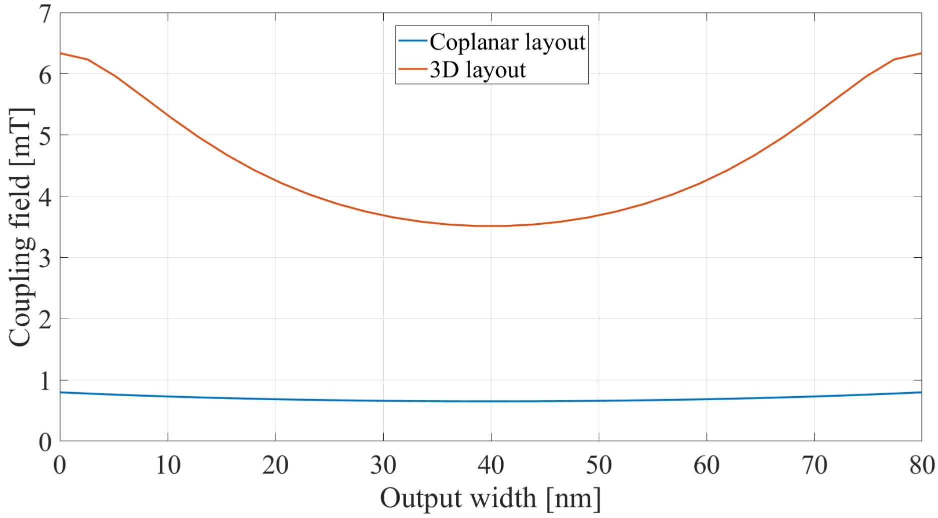

Figure 6.2: *Coupling field comparison: The curves represent the stray field distribution in the output. The stray field generated by the inputs in the 3D layout (red curve) and 2D layout (blue curve) is plotted along the x-direction (width of the output) at the cross section (y=constant) corresponding to the middle of the output.*

Fig.6.1 shows the compared layouts, while fig.6.2 the simulation result. What is plotted is the out of plane component (z-component) of the stray field generated from the inputs along the width of the output (x-direction), at the cross section (y=constant) which corresponds to the center of the output. The red curve is referred to the 3D layout, while the blue to the 2D one. There is a net difference of few mT between the two, which proves that the 3D-stacked layout can be more promising for dipole-coupling based logic computation.

6.1 Sample fabrication and structures patterning

The sample is prepared on a Si substrate with on top 85 nm of SiO_2. By RF magnetron sputtering two layers of Ta/CoFeB/MgO/Ta are deposited, with MgO as interlayer between them. The whole stack is deposited in a single process and the resulting structure with the nominal thicknesses is the following:

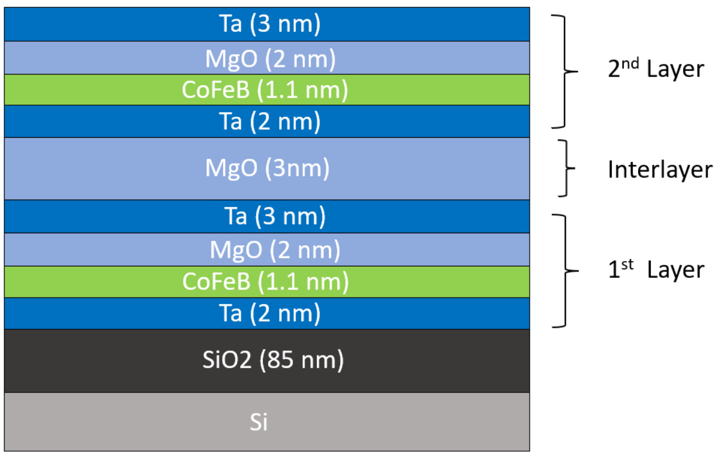

Figure 6.3: *Sketch of the sputtered double layer sample.*

MgO is chosen as interlayer over other material as SiO_2 and HSQ because it can be sputtered with high precision, low roughness and in the same chamber of the other used materials, allowing to deposit all the stack in the same process and avoiding to break the vacuum. The deposition parameters and the thickness of the different layers are the same of the previous sample. The 3 nm thickness of the MgO interlayer is chosen to have 10 nm of distance between the magnetic layers (CoFeB) as in the simulated structure. After the stack deposition, the sample is annealed in N_2 atmosphere at 275 °C for 5 minutes to develop the PMA. The first patterning process is done by photolithography to create a big number of squares (20 μm x 20 μm) on the sample (fig.6.4). After the resist deposition by spin coating and the UV illumination, the structures are physically created by etching the sample via Ar^+ ions. The etching process ($\sim$ 24 minutes) removed both the first and the second layer where unwanted, leaving only the squares.

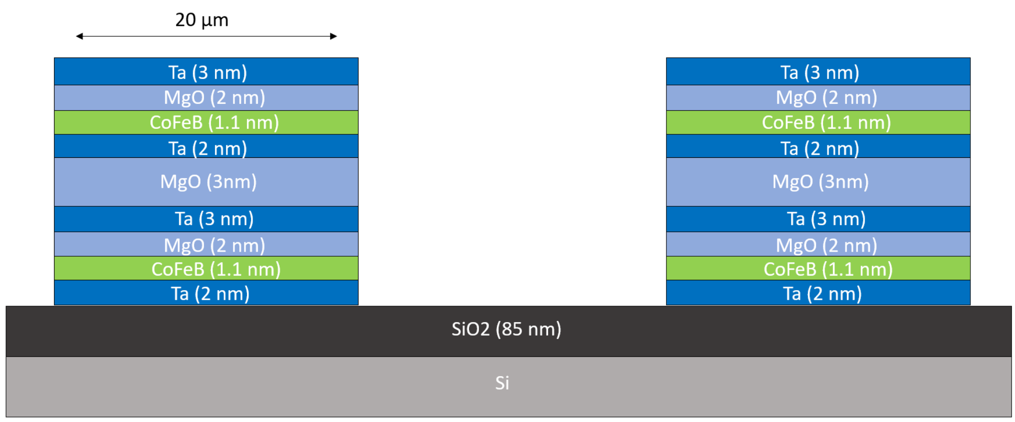

Figure 6.4: *Sketch of the patterned 20 μm x 20 μm squares after the photolithography and the Ar^+ etching process.*

Then, FIB lithography is performed to pattern the islands on the second layer. A PMMA resist ($\sim 35nm$) is deposited by spin coating on the whole sample and illuminated by Ga^+ ions (dose $\sim 3.8 \cdot 10^{12} \frac{ions}{cm^2}$, corresponding to a dwell time of 0.3 μs and a beam current of 2 pA). The irradiation scheme is designed to create the single island and double islands on different squares. After the hard mask evaporation ($\sim 6.5nm$ of Ti) and the lift-off process, the sample is etched by Ar^+ for half time with respect to the previous etching process (i.e, $\sim$ 12 minutes), in order to remove only the first layer and the MgO interlayer. In this way, the islands are created only in the top layer. Some squares instead are not irradiated in such a way to remove the whole second layer and the 3 nm MgO. These simple single layers square are then used to perform the irradiation study and find the correct doses for the areal irradiation and the ANC creation in the output (the complete fabrication recipe with all the parameters is shown in appendix B) . A scheme of the new structures is presented in the following image:

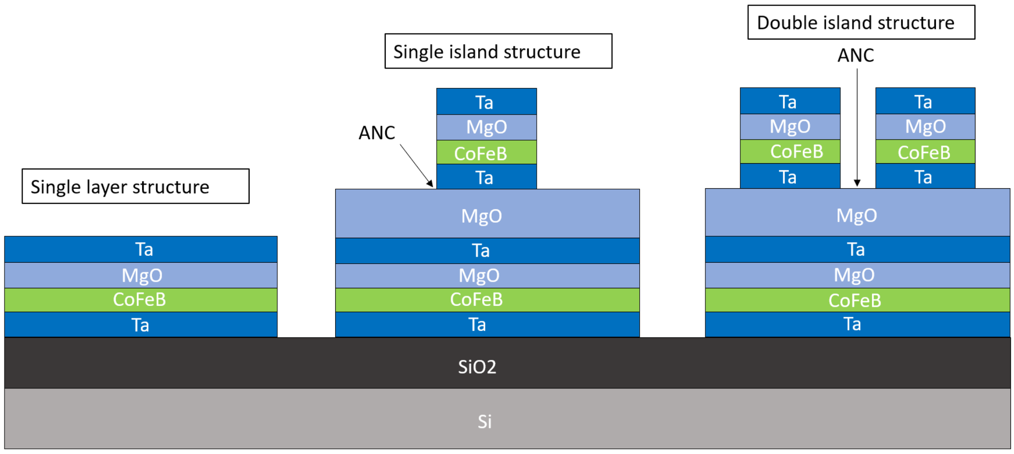

Figure 6.5: *Sketch of the final patterned structures after the FIB lithography and the Ar^+ etching process. From the left to the right: the single input layer structure, used as test structure for the irradiation study, the single island structure and the double island structure.*

Fig.6.5 shows also where the ANCs will be placed to establish the coupling between the two layers. The gap between the two inputs in the double island layout was simulated to be 100 nm. In this experiment different layout with different nominal gaps ranging from 60 nm to 250 nm are patterned. The dimension of the islands is 5 μm x 10 μm. In order to validate the etching process, AFM measurements are performed to check the correct presence of the gap. In particular, in most of the cases, the structures with gap lower than 100 nm show a connection between the two islands. For our applications, a net separation between the two input is necessary. This experiment focuses on the structures with a nominal gap of 150 nm, which should guarantee a clear separation between the inputs, enough space to place the ANC between them, without hit the islands, and enough coupling strength. Fig.6.6 shows an AFM image of the gap of a double island structure with a nominal distance between inputs of 150 nm, while fig.6.7 the corresponding measure, which is estimated to be $\sim$ 152 nm.

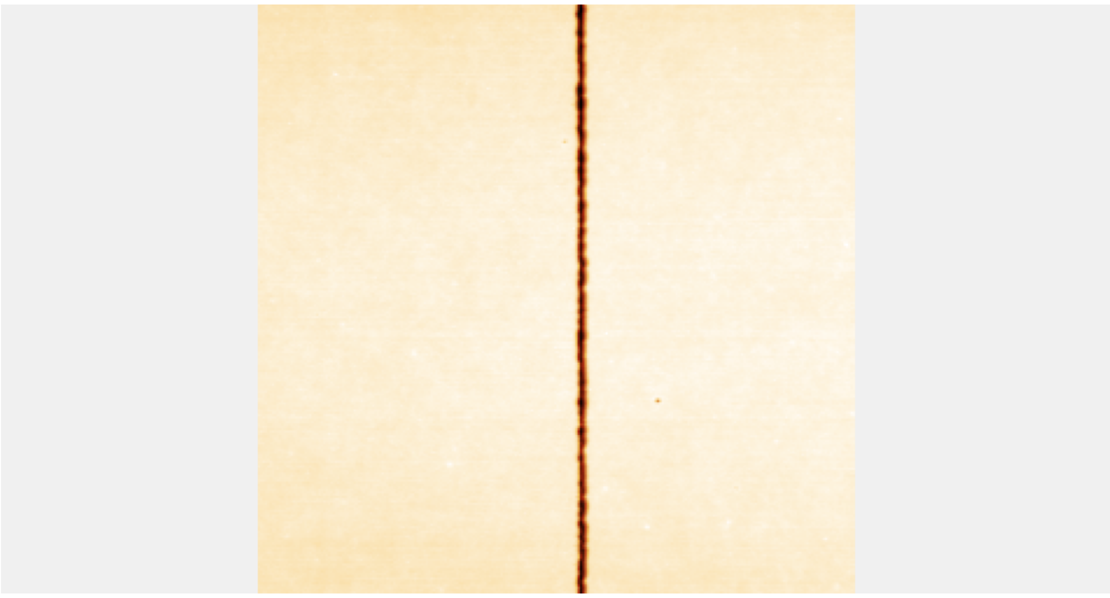

Figure 6.6: *Gap between the two top island imaged by AFM (square A12)*

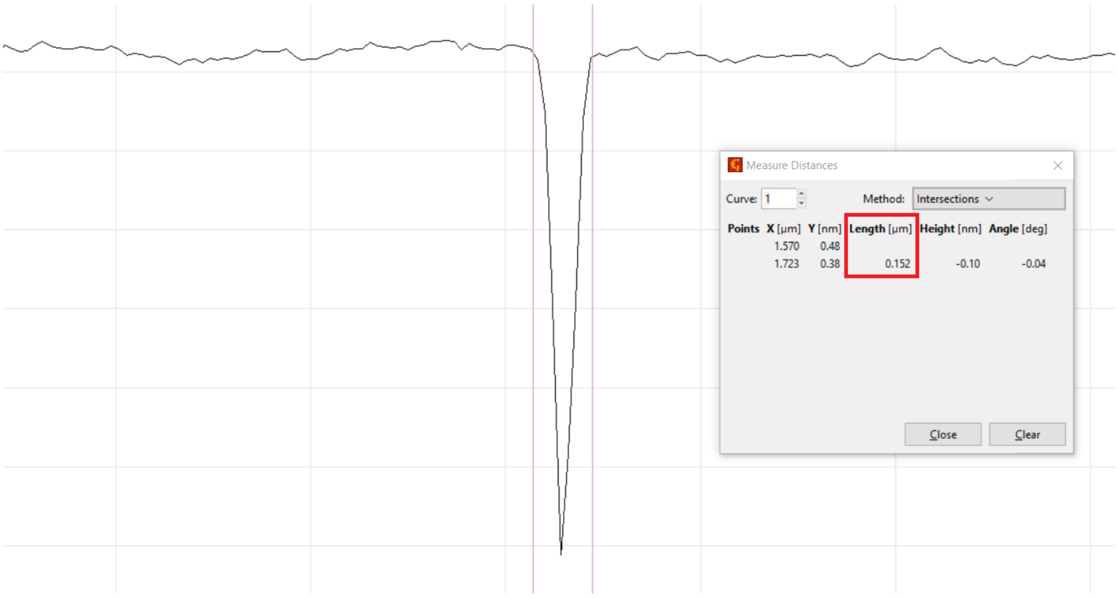

Figure 6.7: *AFM analysis of the gap (square A12). The result shows a measured gap of 152 nm (the nominal distance was 150 nm).*

After the fabrication and the gap check, the structures are measured with the Laser MOKE to analysed the magnetic properties of the different layers. First of all, the hysteresis of a single layer structure is acquired:

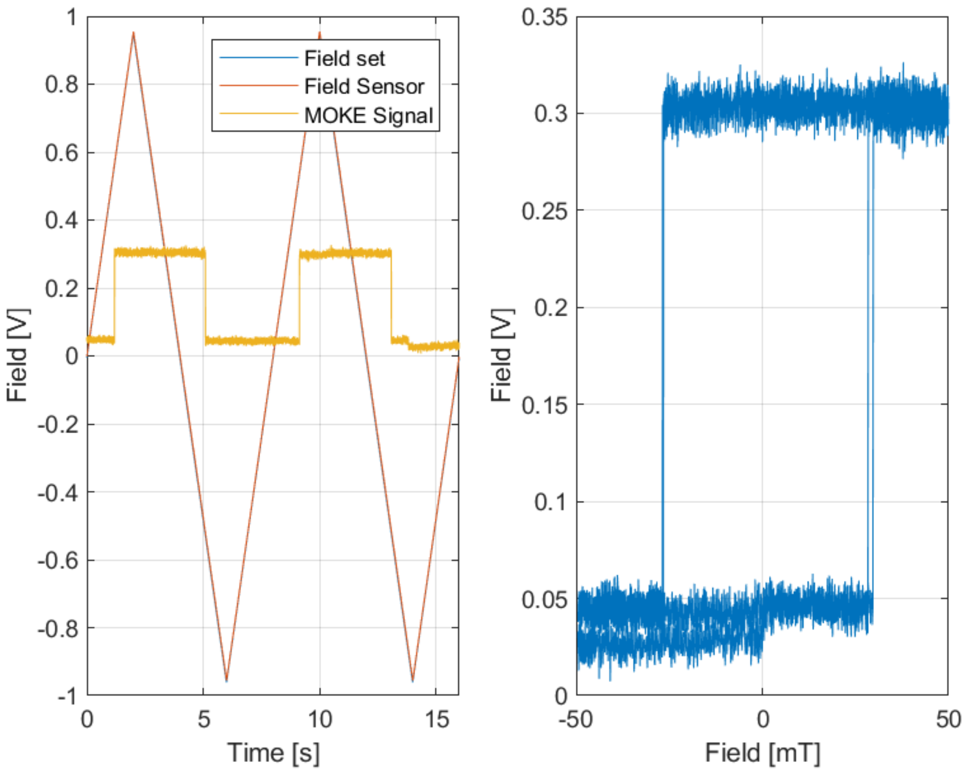

Figure 6.8: *Hysteresis of a single layer structure (square D17). The image on the left represents the output signal of the MOKE and the magnetic field measured by the sensor over the time. On the left instead, the resulting hysteresis.*

The switching field of the single layer structure is found to be ∼ 35 mT. A quite high value compared with the first fabricated structure in section 3. The reason can be found in some different sputtering parameters, like the higher pressure in the main chamber during this deposition with respect to the previous one. Fig.6.9 instead, shows the hysteresis of a single input structure. When an additional layer is introduced, a step appears in the hysteresis. This means a different magnetic behaviour between the top and the bottom one. In this case, a switching field appears at 35 mT, the other at 53 mT. Probably, the first is referred to the bottom one, being equal to the value of the single layer structure, while the second is referred to the input.

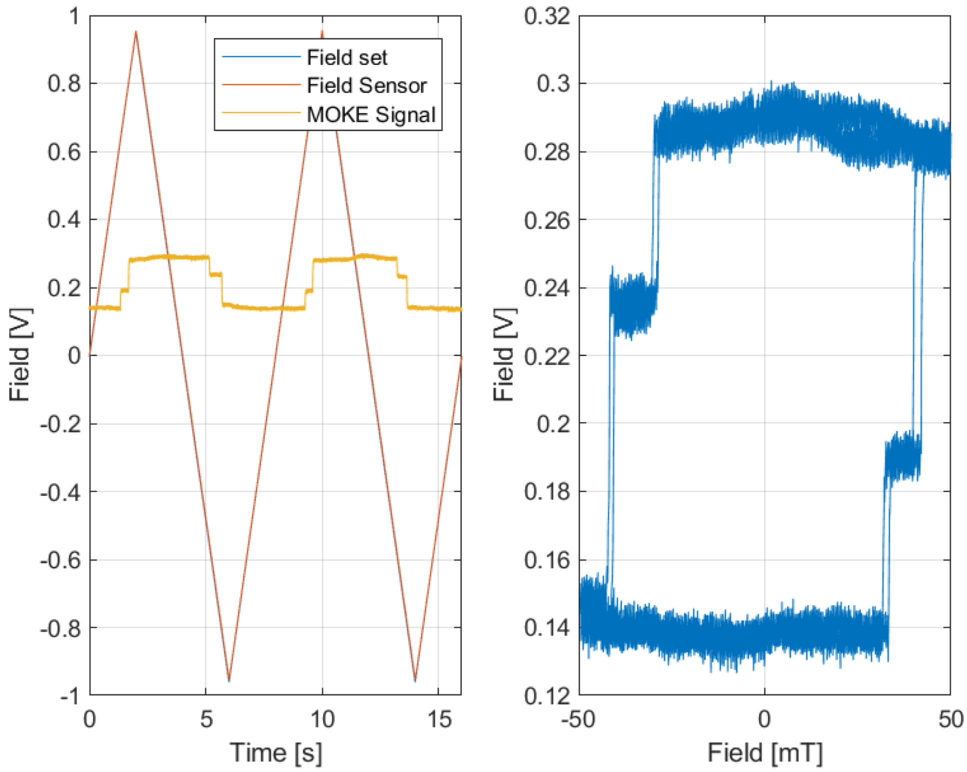

Figure 6.9: *Hysteresis on top of the single island (square C17). The image on the left represents the output signal of the MOKE and the magnetic field measured by the sensor over the time. On the left instead, the resulting hysteresis.*

6.2 Irradiation study

After the verification of the development of the PMA, an irradiation study is performed to find the correct ions doses for the areal irradiation and the ANC creation, which allow to establish the correct coupling between input and output. Due to fabrication variability, the ions doses found in the previous study are no more valid, but they change sample by sample. If one compares fig.6.8 and fig3.2(a), he can see how much different are the magnetic properties between the two samples, which means different crystallographic properties. Hence, also the effect of the ions collisions on the structure changes and a new irradiation study is required. The structures under test are the squares 20μm x 20μm with only a layer of Ta/CoFeB/MgO/Ta (the single layer structures in fig.6.5). These squares did not receive any irradiation during the FIB lithography and for this reason, the etching removes completely the top layer. Their characteristics are equal to the bottom layer of the the single island and double island structures. Hence, equal to the output where the ANC will be created. As already explained in more details in section 4, the switching field before and after the irradiation is studied with a WMOKE.

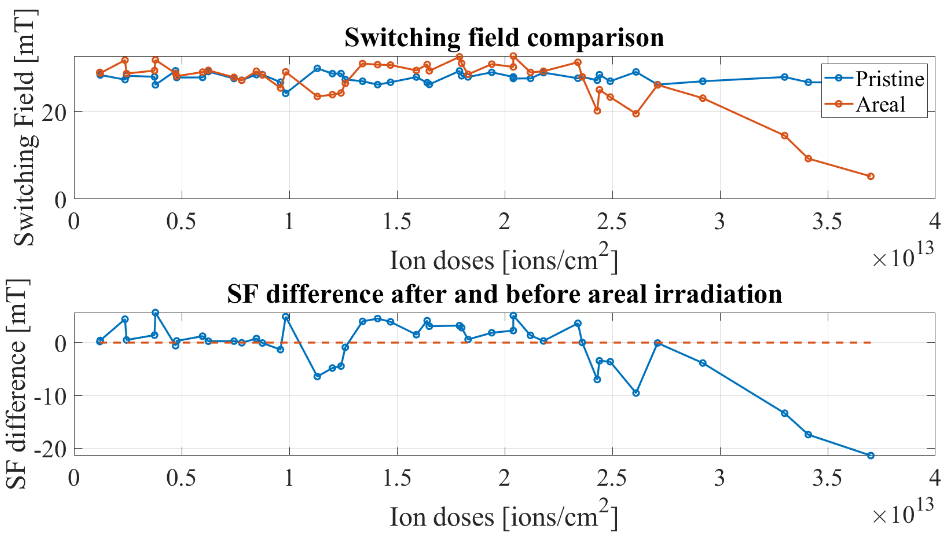

Figure 6.10: *Areal irradiation results: switching field comparison and difference before and after the areal irradiation step, for different ions doses. This irradiation analysis is performed on the single layers structures.*

Fig.6.10 plots the results of the areal irradiation study. Different magnets are irradiated with a different dose and their new switching fields are compared with their values in the pristine state (upper graph). In the bottom graph instead, their difference is plotted. It seems that the right doses are the one from $2.37 - 3.78 \cdot 10^{12} \frac{ions}{cm^2}$ (dwell time: 0.2-0.3 μs) and the ones ranging from $1.34 - 2.34 \cdot 10^{13} \frac{ions}{cm^2}$ (dwell time: 1-1.8 μs). Hence, the region of the plot in which the SF difference curve (bottom graph) is higher than zero. But from this study, it is not really clear which is the best dose for the areal irradiation. An intermediate value belonging to the second group is chosen ($t_{dwell} = 1.5\mu s$) and tested over twenty magnets. The results of this areal irradiation proof test is shown in fig.6.11. Each irradiated magnets (called J00-J19) undergo to an increment in the SF of about few mT, from 1 up to 5 mT. For now, this result is enough and this dwell time is selected and chosen for the next irradiation study.

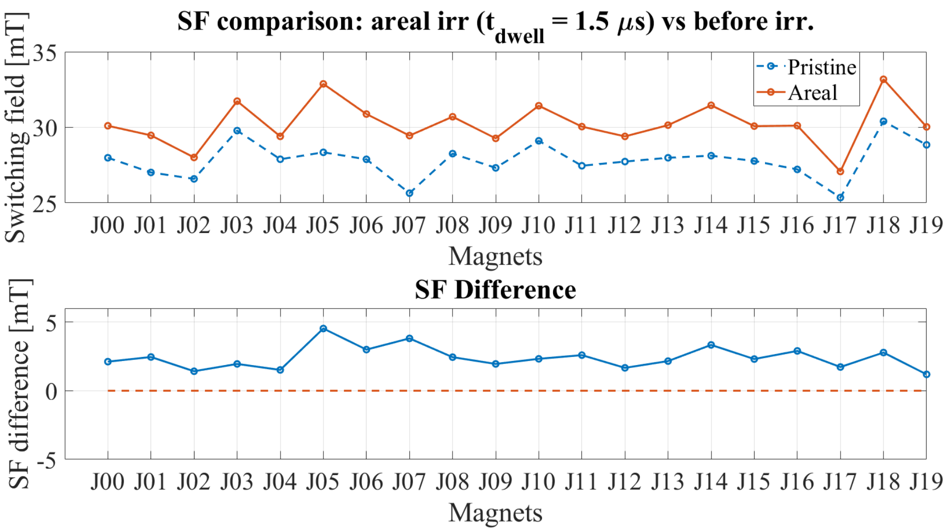

Figure 6.11: *Areal irradiation results: switching field comparison and difference before and after the areal irradiation step, for a selected ion dose ($t_{dwell} = 1.5\mu s$)*

It's worth to say that this result is obtained irradiating an area of the magnet equal to $10\mu m$ x $10\mu m$ instead of the usual $19\mu m$ x $19\mu m$ mask. This because, considering that the size of the tested structure is $20\mu m$ x $20\mu m$, a small misalignment in the irradiation process brings to a shift of the irradiation mask and a consequently overlap of the latter with the edges of the sample. The edges are the sample region richest of defects and even a small amount of ions collisions can be enough to further reduce the anisotropy of these areas in which due to the presence of defects, the anisotropy is already locally reduced. In this way there is a risk to create ANCs where unwanted and to decrease the SF of the whole film, which is not the purpose of this part of experiment.

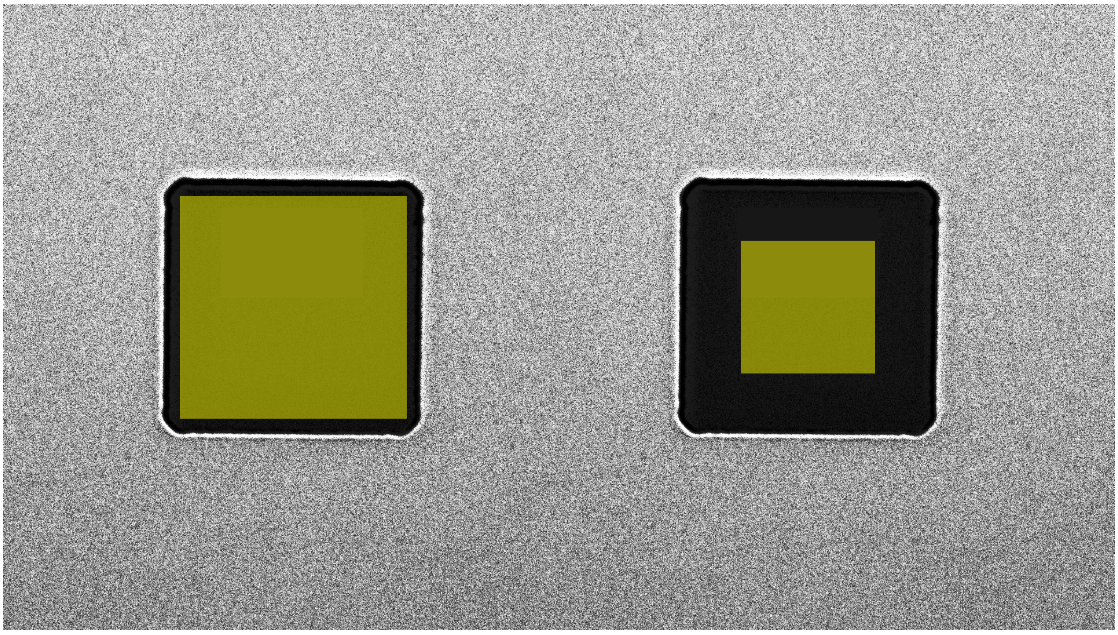

Figure 6.12: *Comparison between two single layer squares with an overlapped mask for FIB areal irradiation of 19 μm x 19 μm (on the left) and one of 10 μm x 10 μm (on the right).*

The ANC study is performed directly on the twenty magnets (J00-J19) already irradiated for a dwell time of 1.5 μs. On each squares an ANC of dimensions 80 nm x 200 nm is created with an increasing dwell time from 1 to 3.9 μs. The same dwell time is used for two consecutive magnets to get rid of exceptions and out of the box behaviours. Fig.6.13 shows the results. The ions doses on the x-axis are the sum of the two irradiation steps. So, the total amount of ions dose in the ANC region. The experiment works and the switching field is reduced up to 13 mT. From this study, the best dwell time which reduce in a effective and stable way the SF of the magnet is 2.7 μs (which corresponds to the points circled in red in fig.6.13), which means a total dwell time of 4.2 μs in the ANC region.

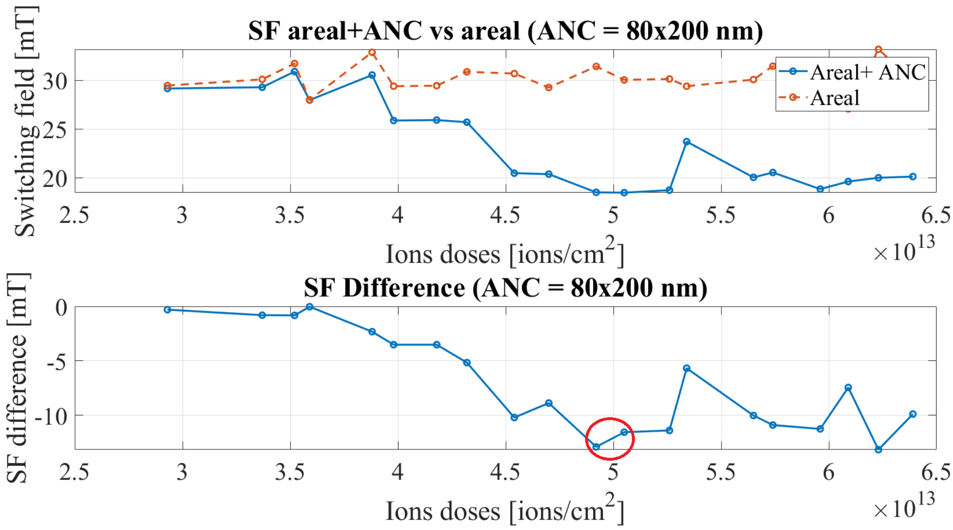

Figure 6.13: *ANC creation results: switching field comparison and difference before and after the ANC creation, for different ions doses. The structures under test are the twenty magnets (J00-J19) already irradiated with an areal irradiation of* $1.5\mu s$ *(fig.6.11)*

With these experiments, the doses for the ANC are ready. These doses will be used in the next experiments to try to reproduce 3D logic devices: an inverter and a double input gate.

6.3 The single input gate

The single input gate is a simple logic structure which consists in a magnetic island (the input) on top of a magnetic layer (the output), separated by an insulating material (MgO). During the FIB lithography of the double sputtered stack (fig.6.3), only an area of $5\mu m$ x $10\mu m$ is illuminated. The result is the evaporation of the hard mask only in this region, leaving both the top and bottom layer in the irradiated area.

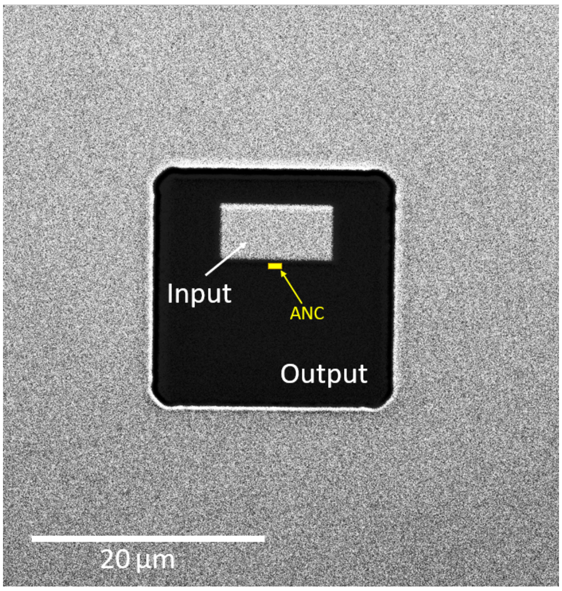

Figure 6.14: *Top view image of the single input device imaged by WMOKE microscope. The yellow arrow indicates where the ANC should be placed.*

In order to have the strongest dipole-coupling possible, the ANC is placed on the output as close as possible to the input (as shown in sketch in figure 6.14). Thanks to the antiferromagnetic coupling, this structure can work as an inverter. When the magnetization of the input and the output are the same, the stray field generated from the first should support the switching of the output inverting its magnetization. To reach this behaviour, the structure needs to be irradiated with the procedure found in the previous study:

- Areal irradiation of both input and output with $\sim 1.85{\cdot}10^{13}\frac{ions}{cm^2}$ ($t_{dwell} = 1.5\mu s$ and beam current = 2 pA)

- 80 nm x 200 nm ANC creation in the output with $\sim 3.2{\cdot}10^{13}\frac{ions}{cm^2}$ ($t_{dwell} = 2.7\mu s$ and beam current = 2 pA)

To verify the validity of the logic function, the Laser MOKE is used to measure the coupling. The measurement steps are:

- To identify the input switching field
- To measure the hysteresis loops of the output for different input logic (1 and 0)

The first device to be analysed is the A4. By positioning the laser spot on the top island is possible to acquire both the switching field of the two layers. From the measurement it results that one switching event happens at 21 mT, while the other at 30 mT. To confirm that is the output the softer magnet, a second hysteresis measurement is done moving the laser spot on the output far from the top island. Fig.6.15 shows the result and confirm that the switching event at 21 mT belongs to the bottom layer.

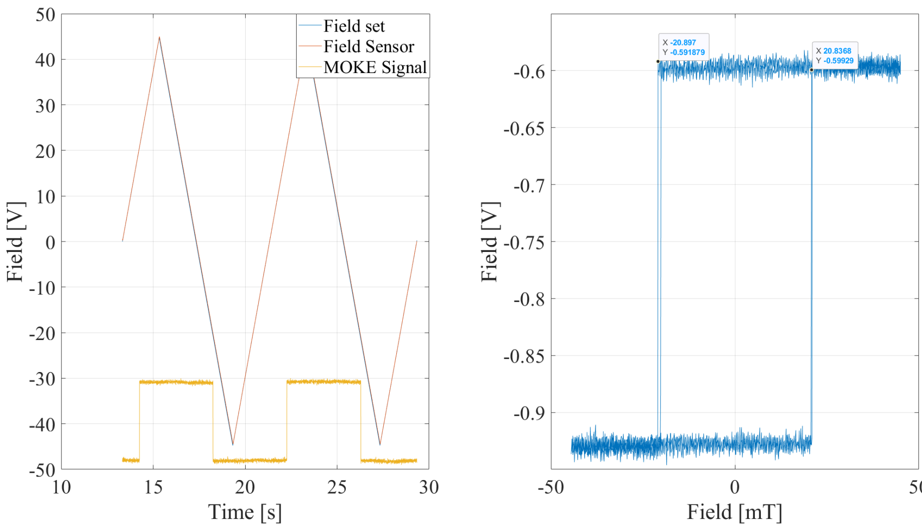

Figure 6.15: *Hysteresis measurement of the bottom layer (sample A4) by Laser MOKE. The image on the left represents the output signal of the MOKE and the magnetic field measured by the sensor over the time. On the left instead, the resulting hysteresis.*

Thanks to the difference in the switching field and to the fact that the input is harder than the output, is possible to fix the input magnetization (logic) with an high field. Then applying lower fields is possible to switch the output, being sure that the input does not switch during the analysis. Hence, to measure the coupling, the top island magnetization is forced to be up (logic = 1) with a positive pulse of 80 mT. Then, fixed the input logic, an hysteresis analysis on the output is performed ranging the field between $\pm 24mT$. The same analysis is done imposing the opposite magnetization to the input (logic = 0). To include statistic, 50 hysteresis loops are measured for every input configurations. Comparing the output switching field (averaged over the 50 measurements) in both the input states and using the formula 5.1 is possible to compute the coupling. The results are shown in fig.6.16. The graph plots all the measured switching events (50 positive and 50 negative) and derives the mean switching value, which depends on the input configuration. When the input magnetization points downwards (logic = 0), the output hysteresis is shifted towards the left. This means that the negative switching field is higher in module than the positive one and so, that it easier for the the output to switch from 0 to 1 inverting the input signal than viceversa. The same happens for the other input configuration, but in the opposite way.

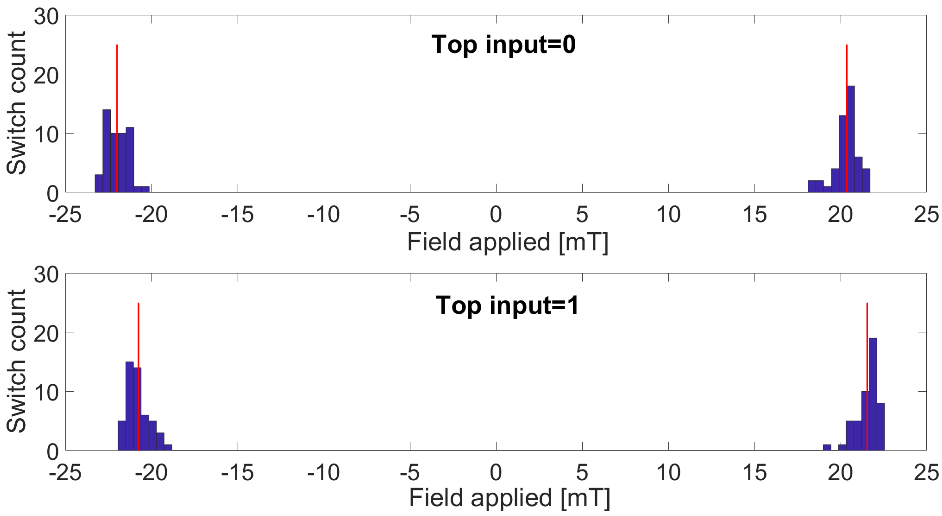

Figure 6.16: *Laser MOKE output 50 cycles hysteresis results for both input logic configurations (sample A4). The blue histograms represent the count of the switching events, while the red line is referred to the mean values of the switching field distribution (indicated as coercivity and defined as* H_c^+ *and* H_c^- *in table 6.1).*

The results are summarized in the following table:

	Input logic = 1	**Input logic = 0**	**Coupling field [mT]**
H_c^+ [mT]	21.54	20.34	0.6
H_c^- [mT]	-20.75	-21.99	0.62

Table 6.1: *Coupling field results (sample A4)*

The same coupling field value are found analysing another sample, meaning that this vary low value (0.6 mT) is not an exception. Probably there was an error in the placement of the ANC, which is not in contact or very close to the top island. But, despite this coupling value is not enough to realize a reliable inverter function (being in the order of magnitude of the thermal switching field), the coupling is clearly demonstrated and an inverter behaviour is obtained.

6.4 The double input gate

The double input gate differs from the previous device only for the presence of a second input. In this case, two areas of size 5 μm x 10μm are illuminated by FIB with a varying distance between them. The ANC is placed in the output in correspondence of the slit between the two top islands. In this way, an anti-ferromagnetic coupling should be established between each of the inputs and the output. The logic equivalent encoded in this structure can be a majority voter considering an external bias as a third virtual input. The experiment is focused on the structures with nominal gap equal 150 nm (fig.6.17).

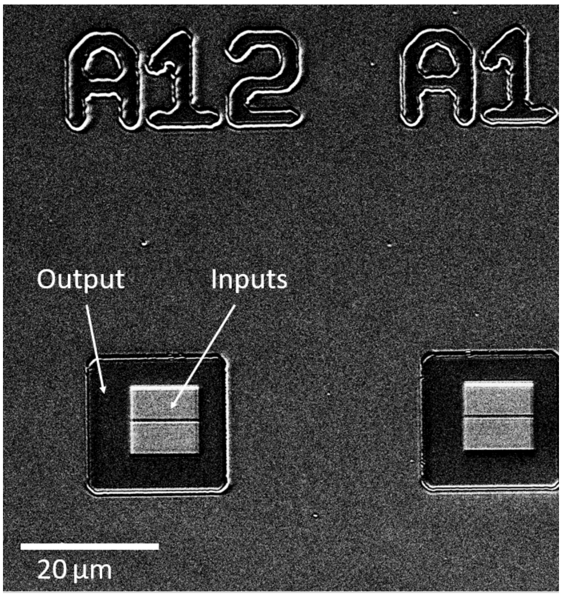

Figure 6.17: *Top view image of two double input devices (called A12 and A13) imaged by WMOKE microscope.*

Two different irradiation plans are applied in this study:

1. First plan:
   - Areal irradiation with $\sim 1.85 \cdot 10^{13} \frac{ions}{cm^2}$ ($t_{dwell} = 1.5\mu s$ and beam current = 2 pA)
   - 80 nm x 200 nm ANC creation in the output with $\sim 3.2 \cdot 10^{13} \frac{ions}{cm^2}$ ($t_{dwell} = 2.7\mu s$ and beam current = 2 pA)

2. Second plan:

    - Areal irradiation with $\sim 1.19 \cdot 10^{13} \frac{ions}{cm^2}$ ($t_{dwell} = 1\mu s$ and beam current = 2 pA)
    - 80 nm x 200 nm ANC creation in the output with $\sim 3.87{\cdot}10^{13} \frac{ions}{cm^2}$ ($t_{dwell} = 3.2\mu s$ and beam current = 2 pA)

The meaning of a new irradiation plan comes from the fact that with an areal irradiation of 1.5 μs the difference in switching field between inputs and output was not enough. To perform correctly all the possible logic combinations is fundamental that this difference is higher than the coupling added with the thermal switching effects. To ensure a correct placement of the ANC in the slit, its position is manually adjusted basing on the image of the structure which comes from the areal irradiation (see the section *Focus ion beam* in A). This means that the areal irradiation hits the edge of the inputs, and if the dose in enough high, it can create nucleation centers that reduce also the switching field of the inputs, decreasing the difference with respect to the output. For this reason, in the second irradiation plan, the dose of the areal irradiation is reduced to 1 μs, while the dose for the creation of the ANC is increased to 3.2 μs (to keep constant the total dose in the ANC region). After the irradiation, the device verification is done as in the previous experiment, exploiting the Laser-MOKE. The steps are:

- To measure the bottom layer hysteresis to check the validity of the ANC
- To measure the top islands hysteresis
- To measure the hysteresis loop of the output for each possible input logic configuration (1,1 ; 0,0 ; 1,0 ; 0,1)

The first sample irradiated following the second plan is the structure A12 (fig.6.17). The measurements (fig.6.18 and fig.6.19) suggest a correct placement of the ANC, three different switching field where recognized. The output switches at $\sim$ 18mT, while the two inputs switch at $\sim$ 28mT and $\sim$ 43mT. To have a great difference between the inputs switching fields is also important because allows to set the inputs configurations 1,0 and 0,1. In these configurations the coupling effects of the two inputs should counteract and the switching behaviour of the output should be the same.

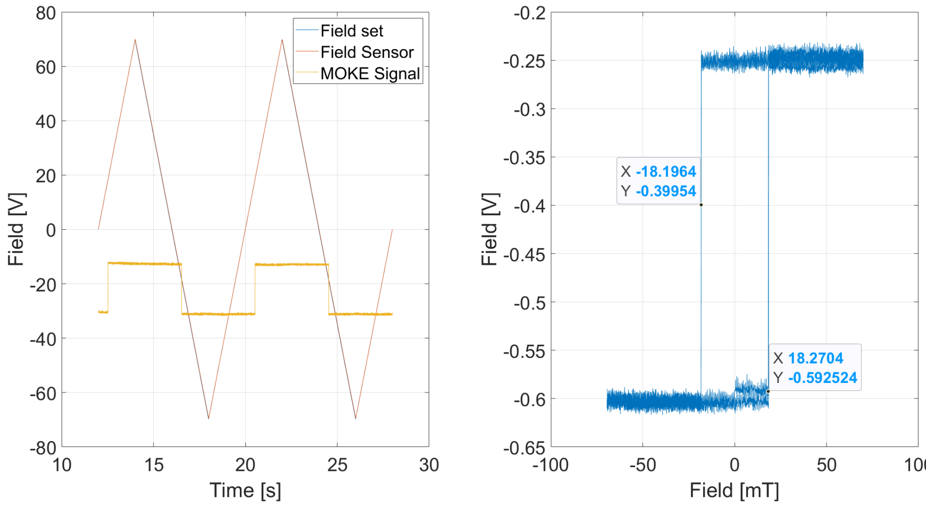

Figure 6.18: *Hysteresis loop measure of the output by Laser-MOKE (sample A12). The image on the left represents the output signal of the MOKE and the magnetic field measured by the sensor over the time. On the left instead, the resulting hysteresis.*

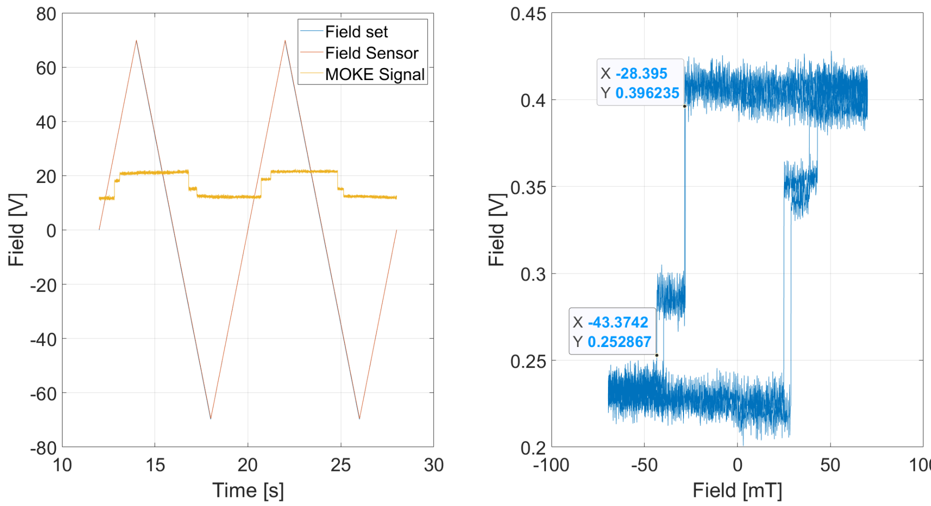

Figure 6.19: *Hysteresis loop measure of the two inputs by Laser-MOKE (sample A12). The image on the left represents the output signal of the MOKE and the magnetic field measured by the sensor over the time. On the left instead, the resulting hysteresis.*

Defined the switching field of inputs and output and so, the measurements limits, the coupling field is computed measuring the 50 hysteresis loops of the output for each of the possible inputs configurations. Before each measurement, a series of pulses is applied to set the desired inputs logic.

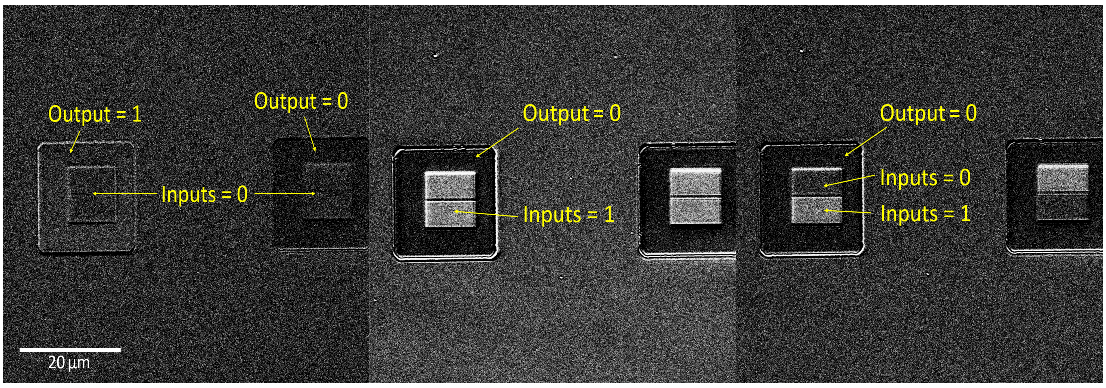

(a) Out = 1, In = 0 (b) Out = 0, In = 1 (c) Out = 0, In1 = 0, In2 = 1

Figure 6.20: *WMOKE images of the sample A12 (the left one) in different logic configurations.*

- **Case 0,1**: To set the desired input logic, two different pulses are applied. A 200 ms pulse of 90 mT to switch to 1 both the inputs and then, a 200 ms negative pulse of -34 mT to switch to 0 the first inputs (the weakest between the two).

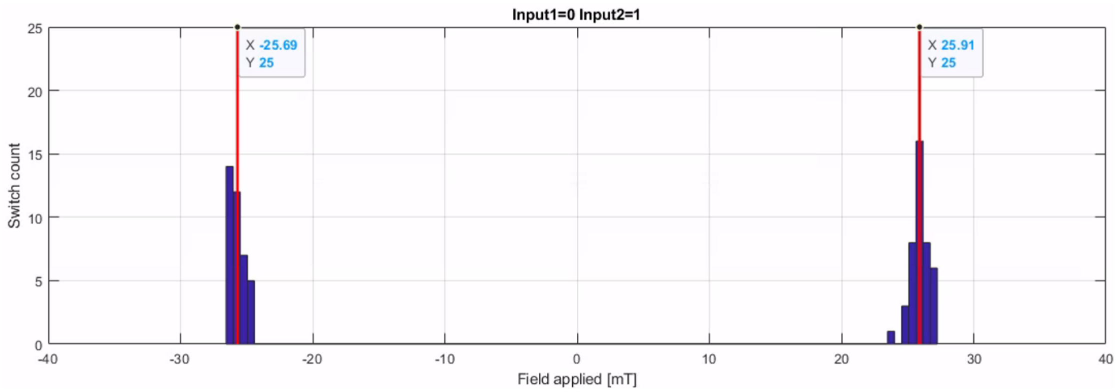

Figure 6.21: *Hysteresis loops analysis: case 0,1. The blue histograms represent the count of the switching events over the 50 hysteresis measurements, while the red line is referred to the mean values of the switching field distribution.*

- **Case 1,0**: To set the desired input logic, two different pulses are applied. A 200 ms pulse of -90 mT to switch to 0 both the inputs and then, a 200 ms positive pulse of 34 mT to switch to 1 the first inputs (the weakest between the two).

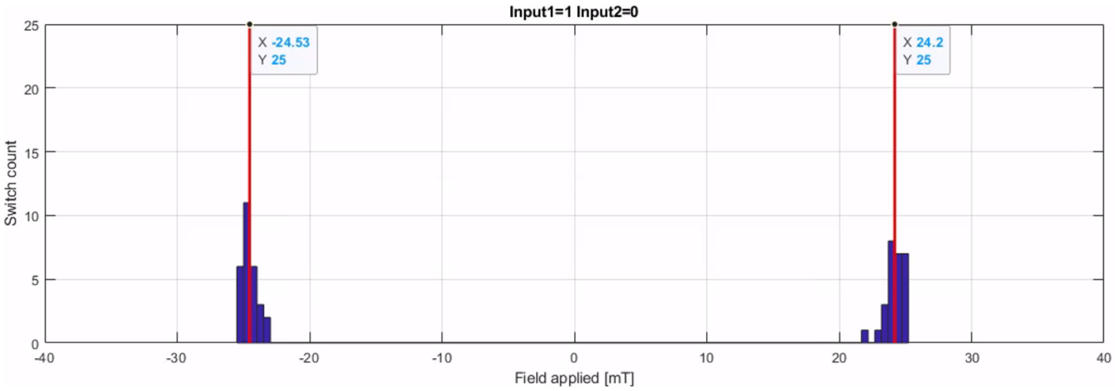

Figure 6.22: *Hysteresis loops analysis: case 1,0. The blue histograms represent the count of the switching events over the 50 hysteresis measurements, while the red line is referred to the mean values of the switching field distribution.*

- **Case 0,0**:

  A 200 ms pulse of -90 mT is applied to switch both the inputs to 0.

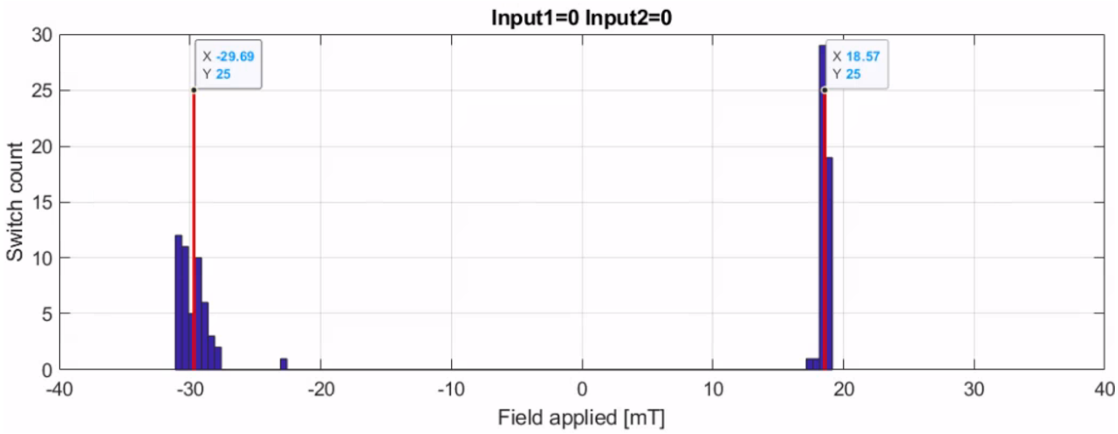

Figure 6.23: *Hysteresis loops analysis: case 0,0. The blue histograms represent the count of the switching events over the 50 hysteresis measurements, while the red line is referred to the mean values of the switching field distribution.*

- **Case 1,1**:

  A 200 ms pulse of 90 mT is applied to switch both the inputs to 1.

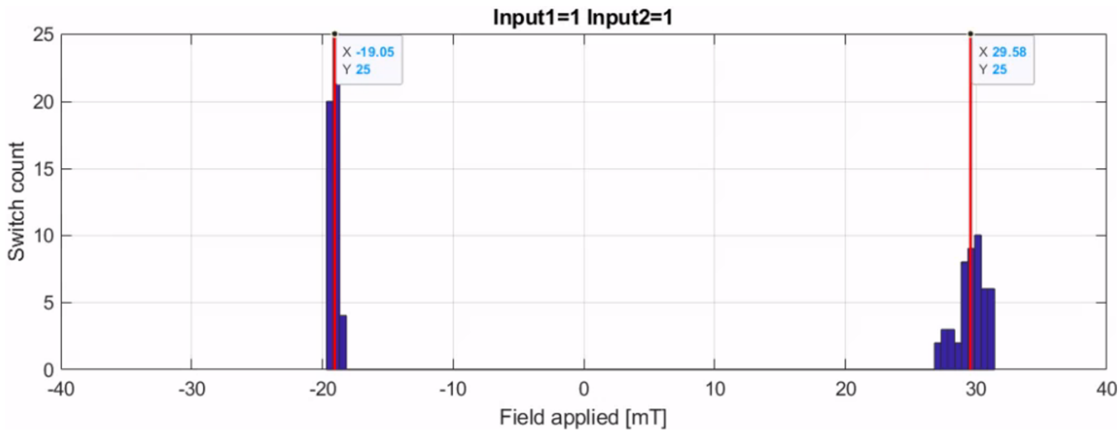

Figure 6.24: *Hysteresis loops analysis: case 1,1. The blue histograms represent the count of the switching events over the 50 hysteresis measurements, while the red line is referred to the mean values of the switching field distribution.*

All the results are summarized in the following table:

Inputs logic	**External field orientation**	**SF mean value [mT]**
11	+ $H_z \Uparrow$	29.58
	- $H_z \Downarrow$	-19.05
00	+ $H_z \Uparrow$	18.56
	- $H_z \Downarrow$	-29.69
10	+ $H_z \Uparrow$	25.9
	- $H_z \Downarrow$	-25.68
01	+ $H_z \Uparrow$	24.19
	- $H_z \Downarrow$	-24.52

Table 6.2: *Coupling field results*

The results show that the expected device function is confirmed. When the inputs logic is opposite (case 1,0 and 0,1), the antiferromagnetic coupling effects counteract cancelling them self, and the hysteresis of the output is almost symmetric. There is still a small difference in the positive and negative value of the output switching fields. Due to unavoidable fabrication inaccuracies, the inputs are not completely equal and the ANC probably is not placed exactly in the middle of the slit and so, a small but negligible unbalance is present. When instead the inputs magnetization point in the same direction (logic 1,1 and 0,0), the dipole-coupling is strong and the output switch is supported in the opposite direction with respect to the inputs magnetization. In this case the hysteresis is no more centered in zero, but it is shifted towards the right (case 1,1) and towards the left (case 0,0). The coupling is computed exploiting the formula:

$$C = \frac{H^{+} - H^{-}}{2} \tag{6.1}$$

The computed coupling fields from the inputs combinations 1,1 and 0,0 are respectively 5.3 mT and 5.5 mT. Both the results confirm a strong coupling in the region of the ANC. This device proves the feasibility to perform a logic computation with more then one input, but does not prove a real logic operation. To have a logic function, a third input must be added. This third input can be a physical magnet (challenging to be physically built in a 3D layout) or a virtual third inputs implemented by a bias field. In this way is possible to create a working 3D denied majority voter. Fixing the bias field is even possible to replicate a NOR and a NAND function, giving the possibility to perform all the basic set of Boolean logic functions.

7 Conclusion

Perpendicular Nanomagnetic Logic is a promising beyond CMOS technology. Thanks to the magnets intrinsic capability to store information in their bistable magnetization states, it provides the possibility to overcome the Von Neumann bottleneck and combine memory and logic computation in the same structure. pNML devices can build ultra low power systems. They don't need a power supply network, the power is only furnished by magnetic clocks. Moreover, they work at room temperature, they are radiation hard and free of leakage currents. All these characteristics can be improved finding the perfect materials to build the device. This work investigated the feasibility to exploit Ta/CoFeB/MgO/Ta stack, where the relevant physic is concentrated in the CoFeB/MgO interface. It has been demonstrated how Focused Ion Beam irradiation with Ga^+ ions tunes the magnetic properties of this stack depending on the amount of ions dose used, allowing a bidirectional manipulation of the magnet switching field. The nucleation mechanism is engineered through the combination of the areal irradiation and the generation of the artificial nucleation center (ANC). This allowed to control the nucleation phenomenon in the output and to reach up to 20 mT of difference in the switching behavior between input and output. Thanks to the presence of the ANC, the switching field of the output can be reduced down to 10 mT, which means an high improvement in the clocking power consumption with respect to the previously investigated materials. The results from the FIB irradiation and nucleation studies were then exploited to build logic devices. Fork-like co-planar inverter structures were patterned and their functionality demonstrated, reaching values of coupling fields up to 7 mT. Moreover, this study investigated the feasibility to produce 3D logic structure. To move the input on a different layer can give the opportunity to increase the on chip density and so, the computing capability of the system. The major result of this thesis is the realization of a 3D double input gate. Its reliability is demonstrated for each of the four possible inputs logic configurations. This kind of structure can work as a majority voter with the addition of a third virtual input as a bias field. Fixing this third input, an AND and an OR function can be implemented. So, it was demonstrated that with Ta/CoFeB/MgO/Ta stack is possible to build all the basic Boolean functions (NOT, AND, OR) with very low value of switching fields. However, to compete with CMOS performances, a lot of further research and studies must be done. Higher resolution fabrication techniques can allow to progressive scale the pNML devices, increasing the on chip density, the coupling fields and the clock frequency due to the lower magnet dimensions.

Appendices

A Experimental set-up

In this appendix it is shown an overview over the experimental set up, focusing on the instrumentation used to measure the magnetic properties, as the magneto-optical microscopies (WMOKE and LMOKE) and on the one used to characterize the device. In this work, the main machine used to pattern the nanostructures and to modify their magnetic properties is the Focused ion beam (FIB).

A.1 Magneto-optical microscopy

The basic principle that allows to study the magnetic structure of a sample by microscopy is the magneto-optical Kerr effect (MOKE). It exploits polarized light reflected by the specimen. Basically, when the light hits the surface of a magnetic material, it is tilted by an angle, called Kerr angle, and the sign of the rotation depends on the direction of the local magnetization. Through a polarizing beam splitter, is possible to split the different contributions of reflected light and get an image of the magnetic domains. In both the set up, an electromagnet is embedded in order to perform switching experiments, to acquire hysteresis or to investigate domain wall motion.

A.1.1 Laser-scanning MOKE

The LMOKE set up uses a red laser diode as light source. The laser beam is focused on a tiny spot and scans all the sample exploiting an X-Y scanner with piezo-actuators. The incident light is linear polarized by a polarizer and focus on the sample by a series of lenses. The reflected light is then splitted in its elementary waves, which encode the information about the local magnetization, and guided to separate photo diodes.

A.1.2 Wide-field MOKE

The WMOKE is not a scanning technique, it differs from the LMOKE for the light source and for the analysis system used. In particular, it exploits a blue LED light as source and a digital camera for imaging.

A.2 Focused ion beam

The FIB is an instrument that can be used for different applications. In this work it is used as high resolution lithography technique to create the nanostructures and to local modify, by ions collision, the crystalline structure and the related magnetic properties of the sample. The version used is the Micrion 9500e system. The ion source is liquid gallium which coats a tungsten needle. To create the ion beam, the source is heated by a current and a drop of gallium is pushed towards the tip of needle. The ions emission is the consequence of a potential difference between the ion source and the extractor electrode, which excites the Ga atoms. This potential difference is called *extraction voltage* and it determines the rate of ions emission. This ions emission can slightly vary over time. A *suppressor* is used to correct these variations and to try to keep the beam current fixed, counteracting the extraction voltage by the application of a positive potential. After the extraction, the ions are accelerated through the column by a potential difference between the source (high positive potential) and the ground. In this set up, the ions are carried out using 50keV *acceleration voltage*. Then, a series of lenses is used to focus the beam. *Lens 1* is a three elements system, in which each element operates at a different potential, with the aim to modify the beam trajectory and focus it on the *beam-limiting aperture*. This aperture limits the diameter of the beam and so the current density. *Lens 2* applies the same principle of Lens 1 but with the aim to focus the beam on the sample. By changing the lens voltages is possible to move vertically up or down the focal plane. Another important component is the *stigmator*, also know as the upper *octopole*. It serves to correct the *astigmatism*, which means to correct the beam cross-section from an ellipse to a circle. This is necessary to allow beam focusing. To switch off and on the beam in a rapid way, a combination of *blanking deflectors* and *apertures* is used. With no potential applied to the blanking deflector, the beam is able to pass through the blanking aperture reaching the Lens 2 and then the sample. If a voltage is applied between the blanking deflectors, the Ga^+ are repelled from the positive plate and attracted and absorbed by the negative one, missing the aperture. This element is also a way to measure the beam current. The FIB system operates in a *raster scanning* way. Each scan line is an array of points called *dwell points*, and the time that the beam irradiates over a certain point is called *dwell time*. The *ion dose*, defined as the amount of ions that hit the sample per unit area, is a function of the beam current, the dwell time and the dwell point spacing. The FIB system can also produce images of the irradiated structure through *secondary emission*. A detector near the sample collects the secondary electrons emitted by sample after the ions collision, and develops an electrical signal proportional to the amount of electrons received.

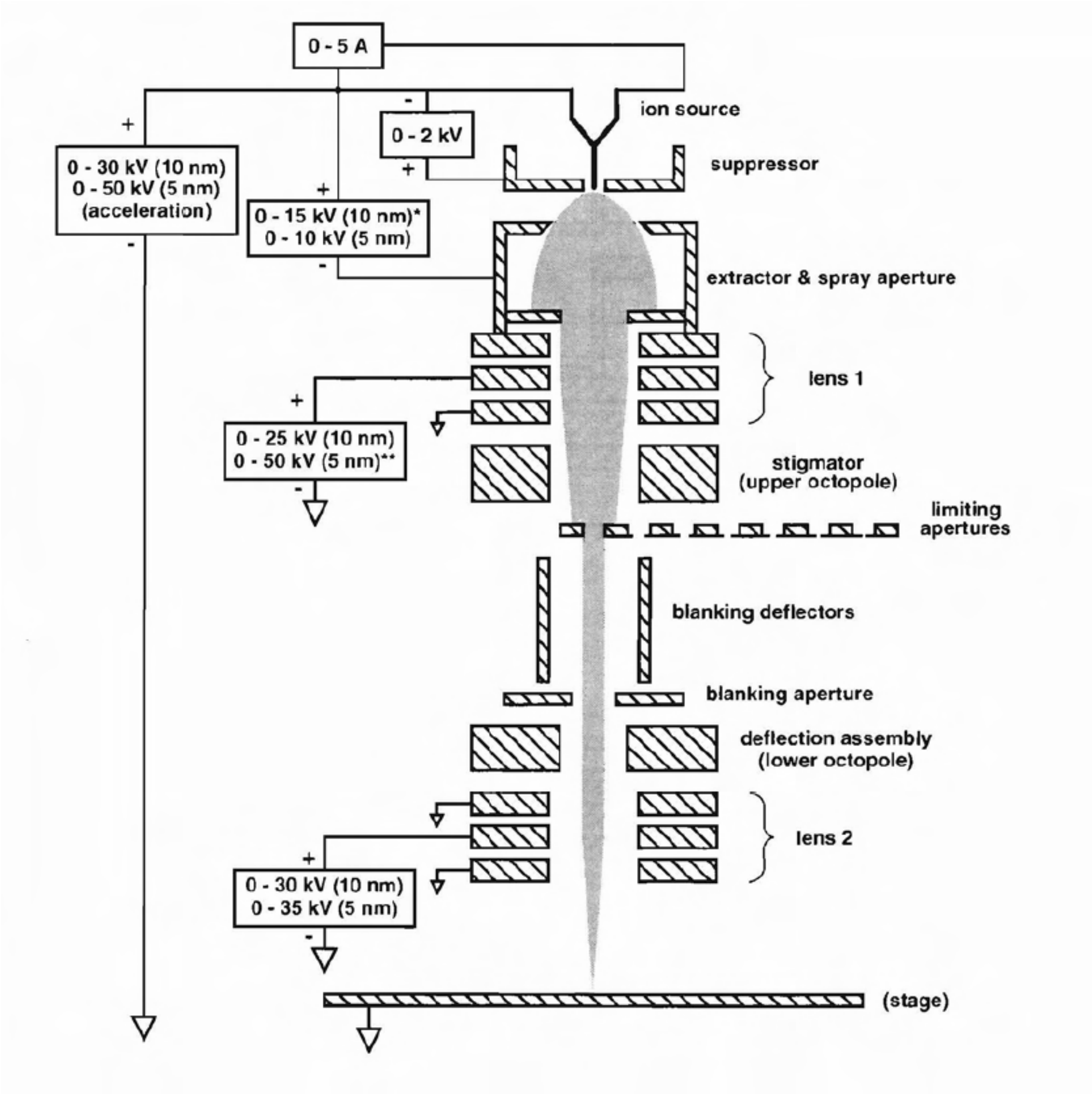

Figure A.1: *Schematic diagram of FIB column architecture (image taken from "Micrion 9000/9100/9.5 00 Focused Ion Beam Systems Operation Manual")*

B Fabrication process parameters

In this appendix are shown in details the fabrication recipes of the structures analysed in this work. All the process parameters are here tabulated.

B.1 2D logic device

This section is referred to the complete fabrication process of the 2D co-planar inverters presented in section 5.

Substrate:

Thermally grown oxide on Si

Material	Thickness
SiO_2	100 nm

Cleaning

Hotplate at 115° for 5 min.

Sputtering:

Initial pressure: $< 3 \cdot 10^{-7}$ bar.
Sputtering parameters:

Material	Power [W]	Pressure [μbar]	Sputter rate [nm/s]
Ta	40	4	0.0457
CoFeB	40	4	0.0279
MgO	40	1	0.006667

Deposited stack:

Layer	Target	Thickness [nm]	Duration [s]
Adesion/Seed	Ta	2	43.7
Magnetic	CoFeB	1.1	39.4
Oxide	MgO	2	300
Capping	Ta	3	65.6

Annealing:

Annealing in controlled atmosphere to develop PMA.

Atmosphere	Temperature [°C]	Time [min]
N_2	275	5

FIB Lithography:

To pattern the fork-like co-planar inverter structure.

Resist deposition

Resist	Spin coat speed [rpm]	Spin coat time [s]	Pre bake T [°C]	Pre bake t [min]	Soft bake T [°C]	Soft bake t [s]
PMMA	1800	30	100	10	100	90

FIB irradiation

Ion	Acc. voltage [keV]	Dwell time [μs]	Beam current [pA]
Ga^+	50	0.3	2

Resist removal

Developer	Time dev [s]	Stopper	Time stop [s]
AZ 600	30	IPA	60

Hard mask evaporation:

Deposition of the etching protecting mask on the whole sample.

Material	Thickness [nm]	rate [A/s]
Ti	6.5	1

Lift-Off:

It removes the remaining resist and the hard mask on top of it, leaving uncovered the region of the sample not illuminated.

Remover	Time [min]	Ultrasonic power	Temperature [°C]
NMP	5	9 (max)	70

Ion etching:

Its the final patterning process, in which all the parts of the sample not covered by the hard mask are removed.

Ion	time [min]	Magnet	Microwave power [W]
Ar^+	12	1086 G	200

B.2 3D Logic device:

The fabrication recipe fro the single input gate and for the double input gate is the same. The devices are patterned on the same double stack sample, what change is only the mask used during the FIB lithography step.

Substrate:

Thermally grown oxide on Si

Material	Thickness
SiO_2	85 nm

Cleaning

Hotplate at 115° for 5 min.

Sputtering:

Initial pressure: $\sim 5 \cdot 10^{-7}$ mbar

Material	Power [W]	Pressure [μbar]	Sputter rate [nm/s]
Ta	40	4	0.0457
CoFeB	40	4	0.0279
MgO	40	1	0.006667

Deposited stack:

Layer	Target	Thickness [nm]	Time [s]
Adesion/Seed	Ta	2	43.7
Magnetic	CoFeB	1.1	39.4
Oxide	MgO	2	300
Capping	Ta	3	65.6
Separation	MgO	3	450
Adesion/Seed	Ta	2	43.7
Magnetic	CoFeB	1.1	39.4
Oxide	MgO	2	300
Capping	Ta	3	65.6

Annealing

Atmosphere	Temperature [°C]	Time [min]
N_2	275	5

Photolithography:

Resist deposition: Spin coating

Resist	Spin coat speed [rpm]	Spin coat time [s]	Pre bake T [°C]	Pre bake t [min]	Soft bake T [°C]	Soft bake t [s]
ECI 3027	4000	60	110	10	110	60

UV exposure - Mask aligner

1. Squared mask to remove excess of resist at the edges:

UV power	Exposure time [s]	Developer	Dev. time [s]
100 %	14	EZ726 MIF	80

2. Patterning of the structures: squares 20μm x 20μm

UV power	Exposure time [s]	Developer	Dev. time [s]
14 %	14	EZ726 MIF	80

Ion etching:

Ion	time [min]	Magnet	Microwave power [W]
Ar^+	24	1086 G	200

Resist removal:

The resist is removed by submerging the sample in a becher containing the stripper solution and putting the bacher in a ultrasonic bath.

Stripper	time [min]	Temperature [°C]	Ultrasonic power
Technistrip P1316	40	65	9 (max)

FIB Lithography:

To create the single and double island in the top layer:

Resist deposition: Spin coating

Resist	Spin coat speed [rpm]	Spin coat time [s]	Pre bake T [°C]	Pre bake t [min]	Soft bake T [°C]	Soft bake t [s]
PMMA	1800	30	100	10	100	90

FIB irradiation

Ion	Acc. voltage [keV]	Dwell time [μs]	Beam current [pA]
Ga^+	50	0.3 G	2

Resist removal

Developer	Time dev [s]	Stopper	Time stop [s]
AZ 600	30	IPA	60

Hard mask evaporation:

Material	Thickness [nm]	rate [A/s]
Ti	6.5	1

Lift-Off:

Remover	Time [min]	Ultrasonic power	Temperature [°C]
NMP	5	9 (max)	70

Ion etching:

Ion	time [min]	Magnet	Microwave power [W]
Ar^+	12	1086 G	200

Bibliography

[1] G. Bertotti. Chapter 6 - micromagnetics. In G. Bertotti, editor, *Hysteresis in Magnetism*, Electromagnetism, pages 163–187. Academic Press, San Diego, 1998. ISBN 978-0-12-093270-2. doi: https://doi.org/10.1016/B978-012093270-2/50055-6. URL https://www.sciencedirect.com/science/article/pii/B9780120932702500556.

[2] S. Blundell. *Magnetism in condensed matter*. Oxford master series in condensed matter physics. Oxford University Press, Oxford, 2001. ISBN 0198505914.

[3] S. Breitkreutz, I. Eichwald, G. Ziemys, D. Schmitt-Landsiedel, and M. Becherer. Influence of the domain wall nucleation time on the reliability of perpendicular nanomagnetic logic. In *14th IEEE International Conference on Nanotechnology*, pages 104–107. IEEE, 2014. ISBN 1479956228.

[4] R. P. COWBURN and M. E. WELLAND. Room temperature magnetic quantum cellular automata. 287(5457):1466–1468, 2000. ISSN 0036-8075.

[5] G. Csaba, P. Lugli, M. Niemier, and W. Porod. Magnetic excitations for information processing. pages 1 – 5, 03 2010. doi: 10.1109/CNNA.2010.5430308.

[6] B. D. Cullity and C. D. Graham. *Introduction to Magnetic Materials*. Wiley-IEEE Press, 2 edition, 2008. ISBN 0471477419.

[7] T. Devolder, I. Barisic, S. Eimer, K. Garcia, J.-P. Adam, B. Ockert, and D. Ravelosona. Irradiation-induced tailoring of the magnetism of cofeb/mgo ultrathin films. *Journal of Applied Physics*, 113(20):203912, 2013. doi: 10.1063/1.4808102. URL https://doi.org/10.1063/1.4808102.

[8] J. H. Franken, M. Hoeijmakers, R. Lavrijsen, J. T. Kohlhepp, H. J. M. Swagten, B. Koopmans, E. van Veldhoven, and D. J. Maas. Precise control of domain wall injection and pinning using helium and gallium focused ion beams. *Journal of Applied Physics*, 109(7):07D504, 2011. doi: 10.1063/1.3549589. URL https://doi.org/10.1063/1.3549589.

[9] A. P. Guimarães. *Priniples of Nanomagnetism*. NanoScience and Technology. Springer, Berlin, Heidelberg, 2009. ISBN 978-3-642-26111-4. URL https://link.springer.com/book/10.1007/978-3-642-01482-6.

[10] Z.-P. Li, S. Li, Y. Zheng, J. Fang, L. Chen, L. Hong, and H. Wang. The study of origin of interfacial perpendicular magnetic anisotropy in ultra-thin cofeb layer on the top of mgo based magnetic tunnel junction. *Applied Physics Letters*, 109(18):182403, 2016. doi: 10.1063/1.4966891. URL https://doi.org/10.1063/1.4966891.

[11] S. Mendisch, F. Riente, V. Ahrens, L. Gnoli, M. Haider, M. Opel, M. Kiechle, M. Ruo Roch, and M. Becherer. Controlling domain-wall nucleation in Ta/Co-Fe-B/MgO nanomagnets via local ga$^+$ ion irradiation. *Phys. Rev. Applied*, 16:014039, Jul 2021. doi: 10.1103/PhysRevApplied.16.014039. URL https://link.aps.org/doi/10.1103/PhysRevApplied.16.014039.

[12] S. Mendsich, V. Ahrens, M. Kiechle, A. Papp, and M. Becherer. Perpendicular nanomagnetic logic based on low anisotropy co/ni multilayer. *Journal of magnetism and magnetic materials*, 510:166626, 2020. ISSN 0304-8853.

[13] H. Meng, W. H. Lum, R. Sbiaa, S. Y. H. Lua, and H. K. Tan. Annealing effects on cofeb-mgo magnetic tunnel junctions with perpendicular anisotropy. *Journal of Applied Physics*, 110(3):033904, Aug 2011. doi: 10.1063/1.3611426. URL https://doi.org/10.1063/1.3611426.

[14] P. Metaxas, J. Jamet, A. Mougin, M. Cormier, J. Ferré, V. Baltz, B. Rodmacq, B. Dieny, and R. Stamps. Creep and flow regimes of magnetic domain-wall motion in ultrathin pt / co / pt films with perpendicular anisotropy. *Physical review letters*, 99:217208, 12 2007. doi: 10.1103/PhysRevLett.99.217208.

[15] N. Miyakawa, D. C. Worledge, and K. Kita. Impact of ta diffusion on the perpendicular magnetic anisotropy of ta/cofeb/mgo. *IEEE Magnetics Letters*, 4:1000104–1000104, 2013. doi: 10.1109/LMAG.2013.2240266.

[16] L.-c. Peng, Y. Zhang, S.-l. Zuo, M. He, J.-w. Cai, S.-g. Wang, H.-x. Wei, J.-q. Li, T.-y. Zhao, and B.-g. Shen. Lorentz transmission electron microscopy studies on topological magnetic domains. *Chinese physics B*, 27(6):66802, 2018. ISSN 1674-1056.

[17] Y. H. e. a. Peng S., Wang M. Origin of interfacial perpendicular magnetic anisotropy in mgo/cofe/metallic capping layer structures. *Scientific Reports*, 5:18173, Dec 2015. doi: 10.1038/srep18173. URL https://doi.org/10.1038/srep18173.

[18] R. Perricone, X. S. Hu, J. Nahas, and M. Niemier. Design of 3d nanomagnetic logic circuits: A full-adder case study. In *2014 Design, Automation & Test in Europe Conference & Exhibition (DATE)*, pages 1–6. EDAA, 2014. ISBN 3981537025.

[19] R. Perricone, X. S. Hu, J. Nahas, and M. Niemier. Design of 3d nanomagnetic logic circuits: A full-adder case study. In *2014 Design, Automation & Test in Europe Conference & Exhibition (DATE)*, pages 1–6. EDAA, 2014. ISBN 3981537025.

[20] R. Perricone, Y. Zhu, K. Sanders, X. Hu, and M. Niemier. Towards systematic design of 3d pnml layouts. In *Proceedings of the 2015 Design, Automation & Test in Europe Conference & Exhibition*, DATE '15, pages 1539–1542. EDA Consortium, 2015. ISBN 9783981537048.

[21] F. Riente, G. Ziemys, C. Mattersdorfer, S. Boche, G. Turvani, W. Raberg, S. Luber, and S. Breitkreutz-v. Gamm. Controlled data storage for non-volatile memory cells embedded in nano magnetic logic. *AIP advances*, 7(5): 55910–055910–5, 2017. ISSN 2158-3226.

[22] F. Riente, S. Mendisch, L. Gnoli, V. Ahrens, M. R. Roch, and M. Becherer. Ta/cofeb/mgo analysis for low power nanomagnetic devices. *AIP Advances*, 10(12):125229, 2020. doi: 10.1063/9.0000013. URL https://doi.org/10.1063/9.0000013.

[23] E. C. Stoner and E. P. Wohlfarth. A mechanism of magnetic hysteresis in heterogeneous alloys. *Philosophical Transactions of the Royal Society of London. Series A, Mathematical and Physical Sciences*, 240(826):599–642, 1948.

doi: 10.1098/rsta.1948.0007. URL https://royalsocietypublishing.org/doi/abs/10.1098/rsta.1948.0007.

[24] R. Tomasello, E. Martinez, R. Zivieri, L. Torres, M. Carpentieri, and G. Finocchio. A strategy for the design of skyrmion racetrack memories. *Scientific reports*, 4:6784, 2014.

[25] G. Turvani, F. Riente, E. Plozner, M. Vacca, M. Graziano, and S. Breitkreutz-v. Gamm. A pnml compact model enabling the exploration of three-dimensional architectures. *IEEE transactions on nanotechnology*, 16(3):431–438, 2017. ISSN 1536-125X.

[26] A. Vansteenkiste, J. Leliaert, M. Dvornik, M. Helsen, F. Garcia-Sanchez, and B. Van Waeyenberge. The design and verification of Mumax3. *AIP Advances*, 4(10):107133, 2014. doi: 10.1063/1.4899186. URL http://doi.org/10.1063/1.4899186.